Alzheimer's Research & Therapy

RESEARCH

Open Access

Rescue of protein dyshomeostasis in hippocampal astrocytes from an Alzheimer's disease mouse model by stabilizing ER-mitochondrial interactions at a 20 nm distance

Giulia Dematteis[1,5†], Chunmei Gong[2†], Justyna Malecka[1], Elisa Tonelli[1,3], Armando Genazzani[4], Laura Tapella[1], Anna Maria Eleuteri[2*†], Dmitry Lim[1*†] and Laura Bonfili[2*†]

Abstract

Background Alzheimer's disease (AD) is the major age-related form of dementia in which dysfunctional ubiquitin-proteasome system (UPS) and autophagy represent primary mechanisms leading to accumulation of misfolded proteins, dysfunction of astroglial cells, neuroinflammation and neurodegeneration. Alterations of the endoplasmic reticulum (ER)-mitochondria contact sites (MERCS), specifically the shortening of the distance between the organelles, was proposed as a key mechanism of cell dysfunction in AD. However, its link to the impairment of the proteolytic system in AD remains unexplored.

Methods We used, as a model, hippocampal astrocytes from 3xTg-AD mice expressing either control plasmid or synthetic linkers stabilizing ER-mitochondrial interaction at 10 nm (10 nm-EML) or at 20 nm (20 nm-EML). Alternatively, astrocytes were treated with mitochondrial Ca^{2+} uptake inhibitor benzethonium chloride or activator amorolfine. We used Western blot to assess protein expression and specific enzymatic activity tests for the analysis of proteasomal, autophagic and lysosomal activities. Single cell fluorescent Ca^{2+} imaging, using 4mtD3cpv probe targeted to the mitochondrial matrix, was used to assess mitochondrial Ca^{2+} uptake.

[†]Giulia Dematteis and Chunmei Gong are co-first authors.

[†]Anna Maria Eleuteri, Dmitry Lim and Laura Bonfili are co-last authors.

*Correspondence:
Anna Maria Eleuteri
annamaria.eleuteri@unicam.it
Dmitry Lim
dmitry.lim@uniupo.it
Laura Bonfili
laura.bonfili@unicam.it

Full list of author information is available at the end of the article

Results Stabilization of MERCS at 20 nm (20 nm-MERCS), which promotes mitochondrial Ca^{2+} uptake, rescued protein ubiquitination, UPS composition and activity. Immunoproteasome components β2i and β5i, upregulated in AD astrocytes, and INFγ, a master-regulator of UPS remodelling in inflammatory conditions, were also rescued. Autophagic markers beclin 1, LC3II and p62, and lysosome-related marker cathepsin B, all upregulated in AD astrocytes, were significantly reduced, while autophagic flux was rescued, by stabilizing 20 nm-MERCS. Furthermore, stabilization of 20 nm-MERCS fully rescued previously reported deficit of mitochondrial Ca^{2+} uptake. Strikingly, application of a mitochondrial Ca^{2+} uptake positive modulator, amorolfine, partially rescued pathological remodelling of UPS and autophagy, suggesting that both mitochondrial Ca^{2+}-related and Ca^{2+}-unrelated mechanisms play a role in the beneficial effect of 20 nm-MERCS stabilization on protein dyshomeostasis.

Conclusions Our results suggest that disruption of ER-mitochondrial interaction is a key factor for AD-related dysregulation of protein degradation and provide a proof that stabilization of MERCS at a defined distance and/or pharmacological rescue of mitochondrial Ca^{2+} uptake represent valuable strategies for the development of future anti-AD therapy.

Keywords Alzheimer's disease, Astrocytes, Proteasome, Immunoproteasome, Autophagy, Lysosomal degradation, ER-mitochondrial contact sites, ER-mitochondrial distance, Mitochondrial calcium uptake, Amorolfine

Background

Alzheimer's disease (AD) is the main form of neurodegenerative disorder representing 70% of age-related dementias. The incidence of AD is constantly growing creating significant social and economic challenge for the society. AD has a complex yet long-lasting pathogenesis. Failure of numerous clinical trials, precluding the development of a disease-modifying therapy, suggests insufficient understanding of molecular mechanisms leading eventually to neurodegeneration. Although senile plaques and neurofibrillary tangles represent histological hallmarks of the AD brain, at the cellular level the primary mechanism driving the accumulation of misfolded and aggregated proteins is the disruption of protein homeostasis—specifically, impairments in proteasomal, autophagic, and lysosomal protein degradation pathways—resulting in the failure of protein clearance [1]. Furthermore, pathologic remodelling of constitutive proteasome in immunoproteasome, triggered by interferon gamma (IFNγ), links protein dyshomeostasis with neuroinflammation, another key aspect of AD pathogenesis [2]. Due to its key role in AD-related proteinopathy, protein degradation machinery represents a promising target for the development of anti-AD therapy.

Astrocytes, main homeostatic cells in the CNS, have recently come to age as important players in AD pathogenesis due to their ability to define neuronal susceptibility to stress and, thereby, the progression of the disease [3]. First of all, astrocytes express all components of amyloidogenic machinery and are able to produce and release β-amyloid (Aβ) peptides, building blocks of senile plaques [4–6]. Therefore, impairment of protein degradation mechanisms in astrocytes, in parallel to neurons, may contribute to AD-related neuropathology [7–11]. Moreover, astrocytes produce and secrete numerous pro-neurogenic and neuroprotective factors promoting neuronal growth and functions [12–14]. Therefore, dysregulation of proteolytic mechanisms in AD astrocytes may compromise their secretome hence homeostatic and defensive functions towards neurons, contributing to neurodegeneration [15–17]. However, little is known about dysfunction of proteolytic mechanisms in AD astrocytes. Recently we reported that in hippocampal astrocytes from an AD mouse model, 3xTg-AD mice, the proteolytic system is dysregulated, which may contribute to the AD-related astrocytic protein dyshomeostasis and loss of homeostatic and protective functions [9].

The interaction sites between organelles, specifically between the endoplasmic reticulum (ER) and mitochondria, represent an important hub for the coordination of fundamental cellular functions such as phospholipid and steroid biogenesis, mitochondrial bioenergetics, apoptosis, protein synthesis and autophagy [18, 19]. ER-mitochondrial contact sites (MERCS) represent highly organized structures that host tethering proteins, and the proteins involved in the above-mentioned functions [20–27]. Transversal distance between the ER membrane and the outer mitochondrial membrane (OMM) and the extension of their interface represent physical parameters, which define the efficiency of processes associated with MERCS [28–30]. Recently, we reported that a specific distance of about 20 nm is optimal for ER-mitochondrial Ca^{2+} transfer and, therefore, for mitochondrial bioenergetics and ATP production [31]. MERCS dysfunction emerges as a key factor in cellular pathophysiology associated with many (if not all) disease conditions including AD and other neurodegenerative diseases [30, 32–34]. In AD, an increased interaction between the ER and mitochondria with a shortening of the transversal ER-mitochondria distance, has been consistently suggested [20, 22–27]. Although in AD astrocytes the link between MERCS dysfunction and protein

dyshomeostasis remains largely unexplored, recent reports from our group suggest that the shortening of the ER-OMM distance may be the leading factor for AD-related astrocytic dysfunction.

First, in line with other reports, we showed that ER-mitochondrial distance is reduced in AD hippocampal astrocytes [35]. Specifically, using a recently developed split-GFP contact site sensor (SPLICS-Short) [36, 37], we observed an enrichment of MERCS at the distance of 8–10 nm. This shortening of ER-mitochondria distance was accompanied with the impairment of both mitochondrial Ca^{2+} uptake and bioenergetics [35]. Next, using a number of cellular types, we showed that the stabilization of ER-mitochondrial interaction at ≈10 nm, using synthetic linkers (ER-mitochondrial linkers, EMLs), inhibited both mitochondrial Ca^{2+} uptake and bioenergetics, while stabilizing the distance at ≈20 nm potentiated mitochondrial Ca^{2+} uptake, oxygen consumption and ATP production, providing a mechanistic link between ER-mitochondrial distance and function [31]. Recently, we found that in immortalized hippocampal astrocytes from 3xTg-AD mice, in line with previous reports from our and other groups, the proteolytic system was strongly dysregulated, including accumulation of ubiquitinated proteins, reduction of 20 S proteasomal activity, IFNγ-dependent conversion of constitutive proteasome to immunoproteasome, and inhibition of autophagic and lysosomal activities [9].

Here we hypothesized that the stabilization of ER-mitochondrial interaction at 20 nm, the distance promoting Ca^{2+} transfer and bioenergetics [31], could be beneficial also for the mitigation of the dysfunction of astrocytic proteolytic machinery.

Methods

Cellular model

Generation of partially immortalized astrocytes from hippocampus of WT and 3xTg-AD mice (WT-iAstro and 3Tg-iAstro cells) has been described elsewhere [38]. Briefly, partially immortalized cell lines were generated from separate primary astrocyte cell cultures deriving from WT and AD mice. To achieve immortalization, primary astroglia cultures were depleted of microglial cells by magnetic-assisted cell sorting using anti-CD11b-conjugated microbeads to obtain a highly purified population of astrocytes. Cells were transduced with retrovirus expressing Simian Virus 40 large T antigen (SVLT). Transformed cells were selected in G418, amplified, and stabilized for 12 passages prior to characterization. No clonal selection was performed to maintain the natural heterogeneity of the cultures. Cells were grown in Dulbecco's modified Eagle's medium (DMEM; Sigma-Aldrich, Cat. D5671) containing 10% fetal bovine serum (Gibco, Cat. 10270) (FBS), 2 mM L-glutamine (Sigma-Aldrich), and 1% penicillin/streptomycin solution (Sigma-Aldrich). Cells were maintained at 37 °C in a 5% CO2 atmosphere. Cells were passaged weekly and used for experiments between passages 12 and 20 after establishment [38].

Plasmids

A 10 nm ER-mitochondrial linker (EML), which fixes the ER-OMM distance at 10–12 nm (denominated as 10 nm-EML), was a kind gift from Dr. György Hajnóczky (Thomas Jefferson University) [28, 39]. Generation and validation of a 20 nm EML (20 nm-EML) was described elsewhere [31] (available from Addgene plasmids ID #231178 and #231181).

Enhanced blue fluorescent protein 2 (EBFP2)-expressing control and 10–20 nm-linker constructs (referred to as ER-BFP, 10 nm-BFP and 20 nm-BFP) were described elsewhere [31] and are available from Addgene (plasmids ID #231183, #231184, and #231185, respectively).

GFP-LC3-RFP probe was a kind gift from Dr. Noboru Mizushima [40] (Addgene plasmid ID #84573).

Cell transfection

For lysates preparation 1×10^6 cells/well (WT- or 3Tg-iAstro) were resuspended in 5 ml of complete DMEM and 5 ml of the transfection mix and plated onto 10 cm^2 dishes. For Calcium imaging experiments 1×10^5 cells/well were resuspended in 1 ml of complete DMEM and 1 ml of the transfection mix and plated onto 24 mm coverslips. For the transfection mix Lipofectamine 2000 (Thermo Fisher Scientific, Cat. 11668-019) and plasmid, in ratio 1:1, were mixed in Opti-MEM (Gibco, Cat. 11058-021); after 3 h, transfection medium was replaced with complete medium. After 48 h, experiments were performed. Routinely, 85–95% of transfection was achieved as detected using fluorescent microscopic analysis.

Cell treatment with both activator and inhibitor of mitochondria Ca^{2+} uniporter (MCU)

WT-iAstro and 3Tg-iAstro cells were plated, and after 24 h were treated with 10 μM of amorolfine (Cat. Y0001795, Sigma) or benzethonium (Cat. 53751, Sigma), MCU activator and inhibitor respectively. Experiments were performed 24 h late.

Preparation of cell lysates

After removing the medium and washing twice with ice-cold phosphate buffered saline (PBS), cells were harvested in PBS and centrifuged at 1600×g for 5 min. The pellet was resuspended with 100 μL lysis buffer containing 20 mM Tris, pH 7.4, 250 mM sucrose, 1 mM EDTA, and 5 mM β-mercaptoethanol, and passed through a 29-gauge needle at least ten times. Lysates were

centrifuged at 12,000×g for 15 min at 4 °C and the supernatants were collected into a 1.5 ml tube and immediately stored at − 80 °C. The protein concentration was quantified through the Bradford method using bovine serum albumin (BSA) as standard.

Measurements of proteasome activities

Proteasome activities were evaluated in cell lysates through fluorometric assays, as previously reported [41], using the following synthetic substrates: Leu-Leu-Val-Tyr-amino-4-methyl-coumarin (AMC) (Sigma-Aldrich, Cat. S6510) for chymotrypsin-like (ChT-L), activity, Leu-Ser-Thr-Arg-AMC (Sigma-Aldrich, Cat. B4636) for trypsin-like (T-L) activity, and Leu-Leu-Glu-AMC (Sigma-Aldrich, Cat. C0483) for peptidyl-glutamyl peptide-hydrolyzing (PGPH) activity. Branched chain amino acid-preferring (BrAAP) activity was measured using Gly-Pro-Ala-Leu-Ala-AMC (Biomatik Corporation, Canada) substrate in the presence of aminopeptidase-N (Sigma-Aldrich, Cat. A8200). The incubation mixture contained the cell lysate (1 µg of total proteins), the appropriate substrate, and 50 mM Tris/HCl pH 8.0, up to a final volume of 100 µL. Incubation was performed at 37 °C, and after 60 min, the fluorescence of the AMC was recorded (AMC, $\lambda_{exc} = 365$ nm, $\lambda_{em} = 449$ nm) on a SpectraMax Gemini XPS microplate reader (Molecular Devices, Sunnyvale, CA, USA). In order to test the 26 S proteasome ChT-L, we used Suc-Leu-Leu-Val-Tyr-AMC as substrate and 50 mM Tris/HCl pH 8.0 buffer containing 10 mM $MgCl_2$, 1 mM dithiothreitol, and 2 mM ATP. The effective 20 S proteasome contribution to short peptide cleavage was evaluated with control experiments performed using specific proteasome inhibitors, Z-Gly-Pro-Phe-Leu-CHO and lactacystin (5 µM in the reaction mixture).

Measurements of cathepsins activities

Cathepsin B and L proteolytic activities were measured following the protocol described by Tchoupè et al. [42] using the fluorogenic peptides Z-Arg-Arg-AMC (Sigma-Aldrich, Cat. C5429) and Z-Phe-Arg-AMC (Sigma-Aldrich, Cat. C9521), respectively, at a final concentration of 50 µM. The mixture, containing 1 µg of protein lysate, was incubated in 100 mM phosphate buffer pH 6.0, 1 mM EDTA and 2 mM dithiothreitol for 1 h at 30 °C. Substrate hydrolysis (AMC, λexc = 365 nm, λem = 449 nm) was detected on a SpectraMax Gemini XPS microplate reader. The effective cathepsins contribution to the proteolysis was evaluated through control experiments performed using the specific inhibitors CA074Me and N-(1-naphthalenylsulfonyl)-Ile-Trp-aldehyde) for cathepsins B and L, respectively.

Western blotting analysis

Cell lysates (20 µg of total proteins) were mixed with the right amount of Laemmli Sample buffer 1x. The samples were resolved by 12% or 15% SDS/PAGE and electroblotted onto PVDF membranes. Membranes with transferred proteins were incubated with the specific primary monoclonal antibody and successively with the proper peroxidase conjugated secondary antibody. Supplementary Table 1 provides detailed information about antibodies used in WB experiments. Clarity Western ECL Substrate was used (Biorad, Cat. 1705061). Detection step was performed on a Biorad ChemiDoc MP imaging system. Each gel was loaded with molecular weight markers in the range of 12 to 225 kDa (GE Healthcare). Glyceraldehyde-3-phosphate dehydrogenase (GAPDH) was utilized as controls for equal protein loading: membranes were stripped and re-probed with anti-GAPDH monoclonal antibody. Stripping buffer contained 200 mM glycine, 0.1% SDS, and 1% Tween 20. ChemiDoc-acquired immunoblot images were processed through Image J software (NIH, USA) to calculate the background mean value and its standard deviation. The background-free image was obtained subtracting the background intensity mean value from the original digital data. The integrated densitometric value associated with each band was calculated as the sum of the density values over all the pixels belonging to the selected band with a density value higher than the background standard deviation. For each band, densitometric value was normalized to the relative GAPDH signal intensity. The ratios of band intensities were calculated within the same Western blot. Calculations were carried out using the Matlab environment (The MathWorks Inc., Natick, MA, USA). Uncropped membranes are presented in Supplementary Material.

Assessment of autophagic flux with GFP-LC3-RFP probe

Generation of stable WT-iAstro and Tg-iAstro cell lines expressing GFP-LC3-RFP probe

Retroviral particles expressing GFP-LC3-RFP probe were generated by transfecting 2×10^6 Phoenix-AMPHO cells (ATCC CRL-3213) with 6 µg pMRX-IP-GFP-LC3-RFP plasmid using 10 µL Lipofectamine 2000 (Thermo Fisher) in a mixture of 1 ml Opti-Mem and 6 ml complete culture medium. 72 h after transfection culture medium was filtered through 0.45 µm filter and concentrated by centrifugation at 5×10^4 xg using an Eppendorf CR30NX centrifuge and R25ST rotor. Viral effective titre was assessed by infecting WT-iAstro cells with serial dilutions and the dilution which gave at least 85% transduced cells was used for the transduction of both WT-iAstro and Tg-iAstro cells plated at a density of 4×10^4 cells/well in a 12 well plate. After three passages transduced cells were used for experiments.

Determination of autophagic flux using GFP-LC3-RFP probe

2×10^4 WT-iAstro or Tg-iAstro cells stably expressing GFP-LC3-RFP probe were plated on 13 mm coverslips (pretreated with 0.1 mg/ml Poly-L-lysine, Sigma) and transfected with either control plasmid (ER-BFP, both lines) or with plasmids expressing 10 nm-BFP or 20 nm-BFP, respectively, and 48 h after transfection were treated either with vehicle (water, 0.1%) or with chloroquine (Sigma, 20 μM final concentration from 20 mM stock prepared in water) for 24 h. After that, cells were fixed in 4% paraformaldehyde, mounted on microscopy slides and analysed using a Leica DMi8 epifluorescent microscope equipped with CoolLED pE4000 light source, HC PL FLUOTAR (340) 40x/1.30 OIL objective, and Hamamatsu Flash 4.0 V3 camera. Images were acquired using LAS-X software. 10–15 fields were taken from each experiment, performed in triplicate. All cells in the field, expressing all three fluorescent proteins, BFP (control plasmid or linker), GFP-LC3 and RFP were counted and the percentage of cells presenting numerous GFP-LC3-positive autophagosomes as compared with cells with diffuse cytosolic GFP localization was determined.

Real-time PCR

Total mRNA was extracted from 1.0 × 10^6 cells 48 h after transfection with control plasmid or linker constructs, using TRIzol Lysis Reagent (Invitrogen, Cat. 15596026) according to manufacturer's instruction. First strand of cDNA was synthesized from 0.5 to 1 μg of total RNA using SensiFAST cDNA synthesis kit (Meridian Bioscience, UK, Cat. BIO-65054). Real-Time PCR was performed using iTaq qPCR master mix according to manufacturer's instructions (Bio-Rad, Cat. 1725124) on a SFX96 Real-time system (Bio-Rad). To normalize raw real time PCR data, S18 ribosomal subunit was used. Data are expressed as fold change compared with WT-iAstro-ER-BFP. Sequences of oligonucleotide primers are present in Supplementary Table 2.

Mitochondrial Ca^{2+}imaging

Mitochondrial Ca^{2+} dynamics were monitored by 4mtD-3cpv sensor, a genetically encoded Ca^{2+} indicator targeted to the mitochondrial matrix [43]. After 48 h transfection, expression of 4mtD3cpv was checked and mitochondrial matrix calcium dynamics were monitored. Coverslips were washed using KRB solution (125 mM NaCl, 5 mM KCl, 1 mM Na_3PO_4, 1 mM $MgSO_4$, 2 mM $CaCl_2$, 5.5 mM glucose, 20 mM HEPES, pH 7.4), transferred to an acquisition chamber, and mounted on the stage of a Leica DMI6000B epifluorescent microscope equipped with an S Fluor 40×/1.3 objective, a Polychrome V monochromator (Till Photonics, Munich, Germany), a Photometrics DV2 dual imager (Teledyne Photometrics, Tucson, US). Samples were illuminated at 420 nm and simultaneously acquired at 475 nm (donor, ECFP) and 530 nm (acceptor, circularly permuted (cp.) Venus) using a Hamamatsu cooled CCD camera. CpVenus/ECFP ratio was calculated online using MetaFluor software. After acquisition of basal Ca^{2+} levels (first 30 s of acquisition), the cells were stimulated with 100 μM ATP. Regions of interest (ROIs) were defined around individual mitochondria.

Statistical analysis

Biochemical data are expressed as mean values ± SEM of at least three independent experiments. Statistical analysis was performed using the one-way ANOVA, followed by the Bonferroni test using the Prism software (GraphPad Prism). The level of significance was set at *p*-values < 0.05 (*), < 0.01 (**) and < 0.01 (***).

Results

Experimental design and samples of the study

To investigate cause-effect relationship between ER-mitochondrial distance and AD-related impairment of proteasomal and autophagic protein degradation we used a well characterized astrocytic cellular model of AD, partially immortalized hippocampal astrocytes from 3xTg-AD mice, denominated as WT-iAstro and Tg-iAstro cells [9, 13, 35, 38] (Fig. 1A). We exploited our recent discovery of the dependence of the ER-mitochondrial Ca^{2+} transfer efficiency on the physical distance between organelles: by overexpressing artificial tethers, we showed that at 10 nm distance (10 nm-EML) Ca^{2+} transfer and mitochondrial function was significantly inhibited, while at 20 nm distance (20 nm-EML, Fig. 1B) mitochondrial Ca^{2+} uptake and OxPhos were potentiated as compared with control plasmid [31]. We transiently transfected WT-iAstro either with control plasmid (ERmRFP) or with 10 nm-EML, while 3Tg-iAstro were transfected with either ERmRFP or with 20 nm-EML (Fig. 1C). 48 h after transfection cells were used for experiments.

20 nm-EML rescues 20 S proteasomal activity and accumulation of ubiquitinated proteins

First, we analysed protein ubiquitination and 20 S proteasomal activity. We observed a markedly downregulated 26 S chymotrypsin-like (26 S ChT-L) activity compared to control WT-iAstro expressing ER-mRFP (WT-ERmRFP). 3Tg-iAstro expressing 20 nm-EML (Tg-20nmEML) showed a significantly increased 26 S ChT-L activity with respect to 3Tg-iAstro cells expressing control ER-mRFP construct (Tg-ERmRFP) (Fig. 2A). Western blotting results showed that the intracellular levels of ubiquitin conjugates were significantly enhanced in WT-10nmEML astrocytes compared to WT-ERmRFP. As expected, accumulation of ubiquitinated substrates occurred in Tg-ERmRFP as a consequence of proteasome inhibition. Interestingly, Ub-conjugated levels were

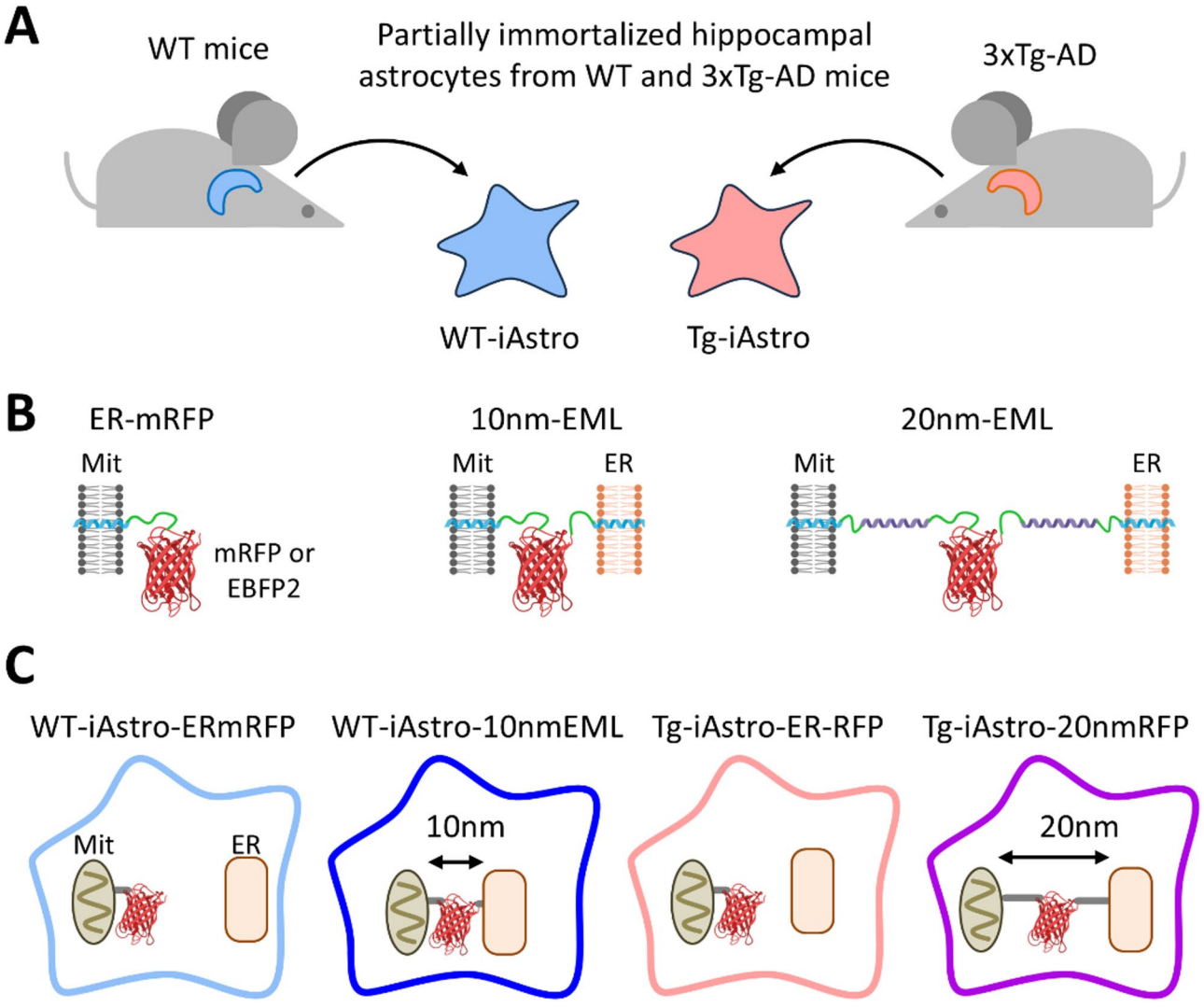

Fig. 1 Scheme depicting study design, ER-mitochondrial linkers and experimental conditions. (**A**) As a cellular astrocytic AD model, partially immortalized hippocampal astrocytes from 3xTg-AD mice were used. (**B**) Linker constructs used in this study were composed of a fluorescent protein (mRFP or EBFP2, here depicted in red) flanked by flexible spacers (green) and by targeting sequences for the outer mitochondrial membrane (OMM) and the ER membrane (light blue helices) at the C- and N-terminal ends of the construct, respectively. To warrant stabilization of the ER-mitochondrial interaction at 20 nm distance, rigid alpha-helical sequences were introduced between targeting sequences and fluorescent protein as described in [31] (violet helices). Control plasmid contained a fluorescent protein targeted to the outer surface of the OMM. (**C**) Scheme depicting experimental conditions tested in this work. WT-iAstro were transfected either with ER-mRFP control construct (light-blue contour) or with 10 nm-EML (blue contour) to mimic shortening of ER-mitochondrial distance found in Tg-iAstro cells [13, 35]. To test if stabilization of ER-mitochondrial interaction at 20 nm would rescue AD-related astrocytic alterations, Tg-iAstro were transfected either with ER-mRFP (control, light-red contour) or with 20 nm-EML (violet contour)

reduced in Tg-20nmEML astrocytes (Fig. 2B), confirming the impact of a proper ER-mitochondrial distance on the functionality of the 26 S proteasome and indicating that stabilization of ER-mitochondrial interaction at 20 nm can be a valuable strategy to rescue proteasome enzymatic functionality in the AD cellular phenotype.

In order to assess the functionality of the 20 S proteasome, enzymatic assays using specific synthetic fluorogenic substrates were performed. ChT-L and T-L activities of the 20 S proteasome, which are typically attributed to β5 and β2 catalytic subunit respectively [44], were significantly downregulated in WT-10nmEML cells compared to WT-ERmRFP cells. In contrast, both ChT-L and T-L were significantly increased in Tg-20nmEML cells compared to Tg-ERmRFP cells. The BrAAP activity was significantly reduced in WT transfected with the 10-nm linker (WT-10nmEML), mimicking the AD condition (Tg-ERmRFP), while BrAAP activity was rescued in Tg-20nmEML. No significant difference was observed in PGPH activity, which is constitutively attributed to the β1 subunit (Fig. 2C).

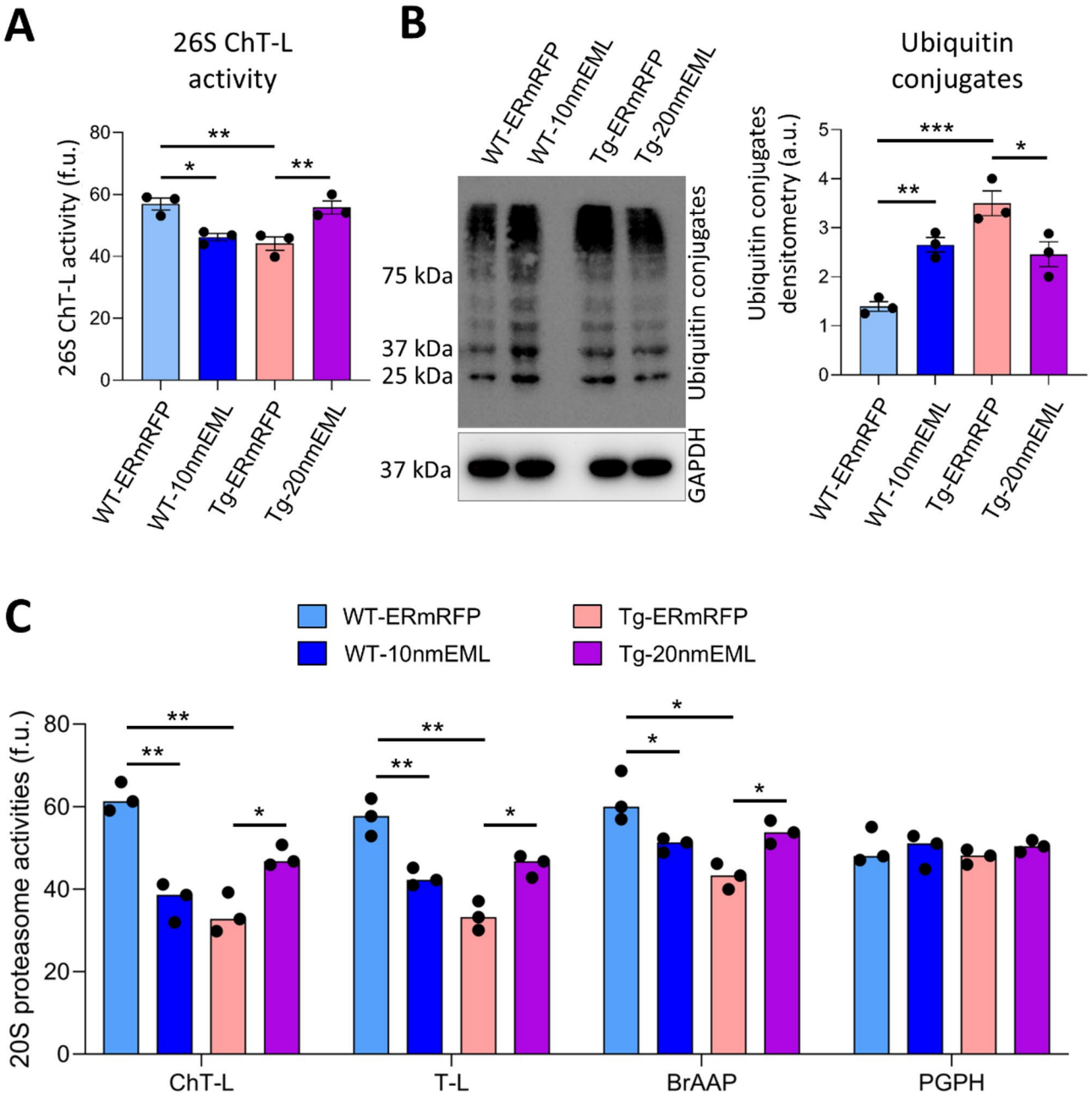

Fig. 2 Rescue of UPS function by 20 nm-EML in AD astrocytes. WT-iAstro were transfected with ER-mRFP or 10 nm-EML; Tg-iAstro were transfected with ER-mRFP or 20 nm-EML. 26 S ChT-L proteasomal activity (panel **A**). Representative immunoblot of ubiquitin conjugates (panel **B**) and densitometry normalized by GAPDH, expressed as arbitrary units (a.u., mean ± SEM, from three independent experiments). Panel (**C**) 20 S proteasomal activities measured through enzymatic fluorometric assays. ChT-L, T-L, BrAAP, and PGPH mean ± SEM activities are expressed as fluorescence units (f.u.) Data are from three independent subgroups of astrocytes at the same passage number are represented (*$p < 0.05$, **$p < 0.01$, *** $p < 0.001$, according to one-way ANOVA, followed by the Bonferroni test)

It is well known that a specialized form of proteasome named immunoproteasome is assembled in response to cellular stress. In the immunoproteasome the constitutive catalytic subunits β1, β2 and β5 are replaced by the inducible subunits β1i, β2i and β5i providing altered peptide cleavage properties [45, 46]. To assess proteasomal dynamic structure in altered and restored MERCS distances, the subunit compositions of astrocytes was analysed. In line with our recently published report [9], Western blotting showed that the expression level of the constitutive β2 and β5 subunits were markedly reduced in WT-10nmEML cells and in Tg-ERmRFP cells compared with WT-ERmRFP cells. The expression of the 20 nm linker in AD astrocytes (Tg-20nmEML) rescued

the protein expression of both β2 and β5 in respect to Tg-ERmRFP cells (Fig. 3A).

In line with our previous report, β2i and β5i expression levels were significantly higher in WT 10 nm-EML cells and in Tg-ERmRFP cells compared with WT-ERmRFP cells. Strikingly, transfection with the 20 nm linker rescued the protein expression of both β2i and β5i in Tg-20nmEML cells with respect to Tg-ERmRFP cells (Fig. 3A).

We also found that IFNγ, the major mediator of immunoproteasome induction [47, 48], was upregulated in WT-10nmEML, mimicking the AD phenotype and in agreement with the induction of the immunoproteasome upon shortening MERCS distanced. IFNγ levels were restored in Tg-20nmEML compared to Tg-ERmRFP cells (Fig. 3B). Altogether, these results indicated that stabilizing the distance between endoplasmic reticulum and mitochondria at 20 nm can partially restore both the structure and the functionality of UPS.

Modulation of INFγ and inducible proteasome by the stabilization of ER-mitochondrial interaction is transcriptionally regulated

Conversion of the constitutive proteasome to the immunoproteasome occurs under the transcriptional control of INFγ, which, in turn, is regulated at a transcriptional level [49]. Therefore, it was important to investigate if the upregulation of INFγ in 3Tg-iAstro and in WT-10nmEML, and rescue of INFγ protein in Tg-20nmEML astrocytes was transcriptionally regulated. Figure 4A shows that in 3Tg-iAstro cells expressing control plasmid (Tg-ERmRFP), the level of INFγ transcript was increased by more than threefold compared to WT-ERmRFP astrocytes. WT-iAstro transduced with 10 nm-EML (WT-10nmEML) showed significant increase of INFγ transcript by 1.3-fold. Strikingly, 3Tg-iAstro transduced with 20 nm-EML (Tg-20nmEML) strongly reduced and fully rescued the transcription of INFγ RNA (Fig. 4A). The levels of the inducible β1i and β5i transcripts were also significantly higher in Tg-ERmRFP compared with WT-ERmRFP astrocytes and this increase was reproduced by expression of 10 nm-EML in WT-iAstro (Fig. 4B, D). The levels of β2i were not significantly different between WT-ERmRFP and Tg-ERmRFP due to high variability between samples. Strikingly, in line with Western blot results, 20 nm-EML expressed in 3Tg-iAstro strongly reduced and rescued the mRNA levels of all three inducible subunits (Fig. 4B, C,D). Interestingly, we did not find linker-dependent changes, coherent with protein levels, in the expression of transcripts coding for constitutive proteasomal subunits β1, β2 and β5, suggesting that their upregulation in Tg-iAstro occurs at a post-transcriptional level (Supplementary Fig. 1A, B,C).

Rescue of autophagic and lysosomal degradation by 20 nm-EML in AD astrocytes

MERCS regulate a variety of intracellular biological processes including autophagy [18, 50] and modification of MERCS distances can affect the formation of the autophagosome [50, 51]. To examine the functionality of the autophagic pathway in altered or restored MERCS, we first detected the expression levels of autophagy markers such as beclin 1, LC3II and p62. As shown in Fig. 5, significantly increased expression levels of beclin 1, LC3II and p62 proteins in WT-10nmEML cells compared to WT-ERmRFP cells were observed, indicating a defective autophagic flux upon shortening of MERCS distances, recapitulating the same alterations previously observed in in 3Tg-iAstro [9]. Interestingly, higher levels of beclin 1, LC3II and p62 were detected in Tg-20nmEML, suggesting a restored autophagic function upon reestablishing the optimal MERCS distance. Next, we examined the expression level and activity of both cathepsin B and L, which are key cysteine proteases responsible for protein turnover in the lysosomal cellular compartment [52]. In particular, cathepsin B has a role in the deposition of amyloid plaques [53], while cathepsin L has previously been shown to be involved in the proteolytic processing of amyloid aggregates [54]. Significantly increased expression levels (Fig. 6A) and activity (Fig. 6B) of cathepsin B were observed in WT-10nmEML as well as in Tg-ERmRFP cells compared to control cells. Moreover, cathepsin B activity and expression level significantly decreased in Tg-20nmEML cells with respect to Tg-ERmRFP cells, indicating that altering MERCS distances can effectively rescue autophagic flux in AD astrocytes. However, no significant changes were found in both activity and expression levels of cathepsin L in none of the experimental group (Fig. 6). Real-time PCR analysis did not reveal linker-dependent changes, coherent with protein levels, in the levels of transcripts coding for autophagic marker Beclin1 or for proteolytic enzymes Cathepsins B and L, suggesting their posttranscriptional regulation (Supplementary Fig. 1D, E, F).

Collectively, these results support the hypothesis that 20 nm MERCS stabilization exerts beneficial effect on AD-related protein dyshomeostasis in astrocytes [55].

Autophagic flux is impaired in AD astrocytes and is partially rescued by 20 nm-EML

To investigate if changes in autophagy-related proteins may be linked to altered autophagic flux, we used a recently developed fluorescent probe GFP-LC3-RFP to follow the formation of autophagosomes in presence of a lysosomal inhibitor, chloroquine (CQ) [40]. GFP-LC3-RFP fusion protein, expressed in the cell, is processed by the endogenous ATG4 family proteases that cleave the peptide bond after the C-terminal glycine of LC3 in

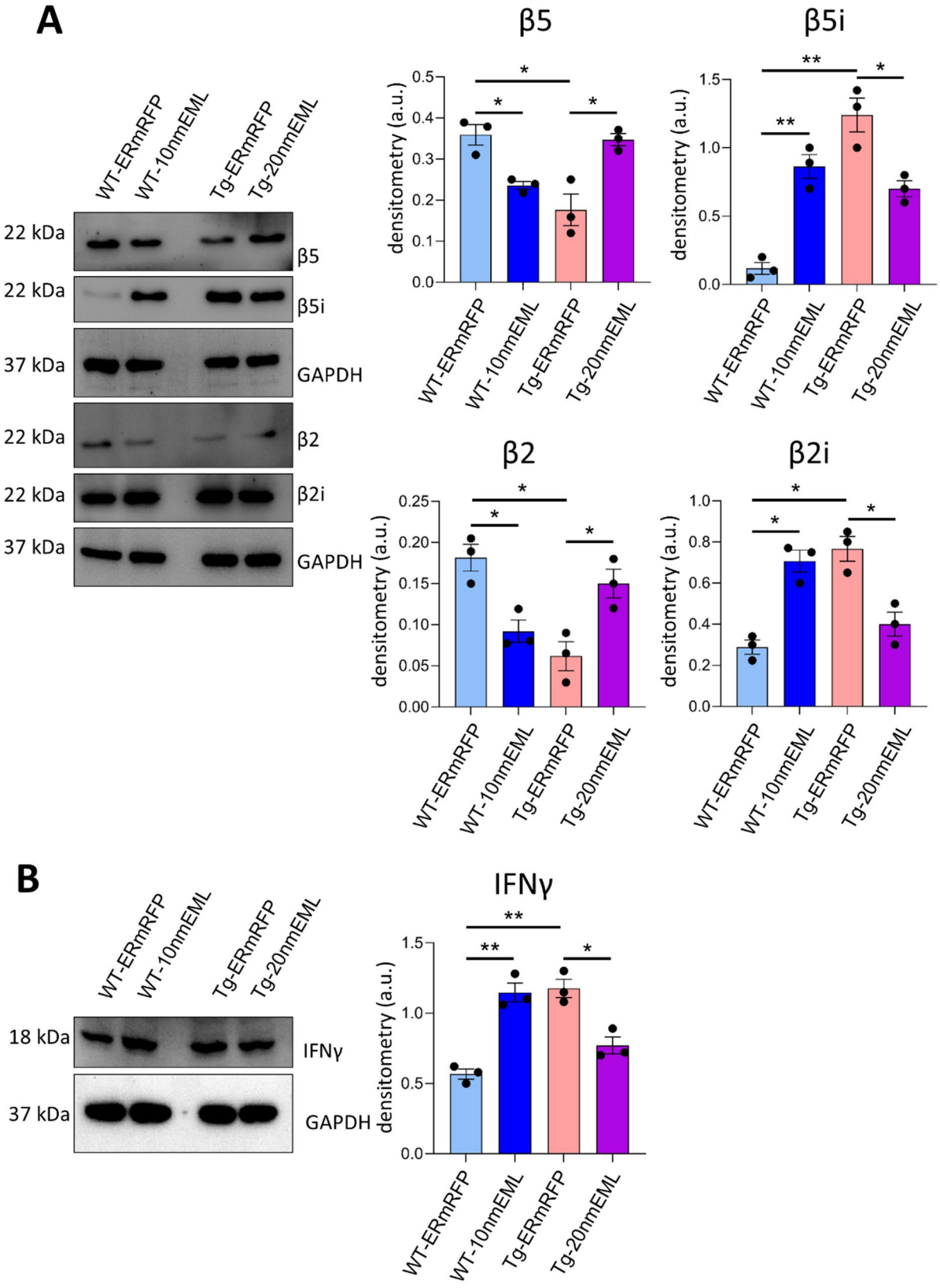

Fig. 3 Rescue of UPS composition by 20 nm-EML in AD astrocytes. Representative Western blots of β5, β5i, β2, and β2i proteasomal subunits (**A**) and IFNγ protein levels (**B**) in WT-iAstro (transfected with ER-mRFP or 10 nm-EML) and Tg-iAstro (transfected with ER-mRFP or 20 nm-EML). For each target protein, the densitometric analysis is reported; it is normalized by GAPDH and expressed as mean ± SEM arbitrary units (a.u.) from three independent experiments. Detection was executed by ECL (*$p < 0.05$, **$p < 0.01$ one-way ANOVA, followed by the Bonferroni test)

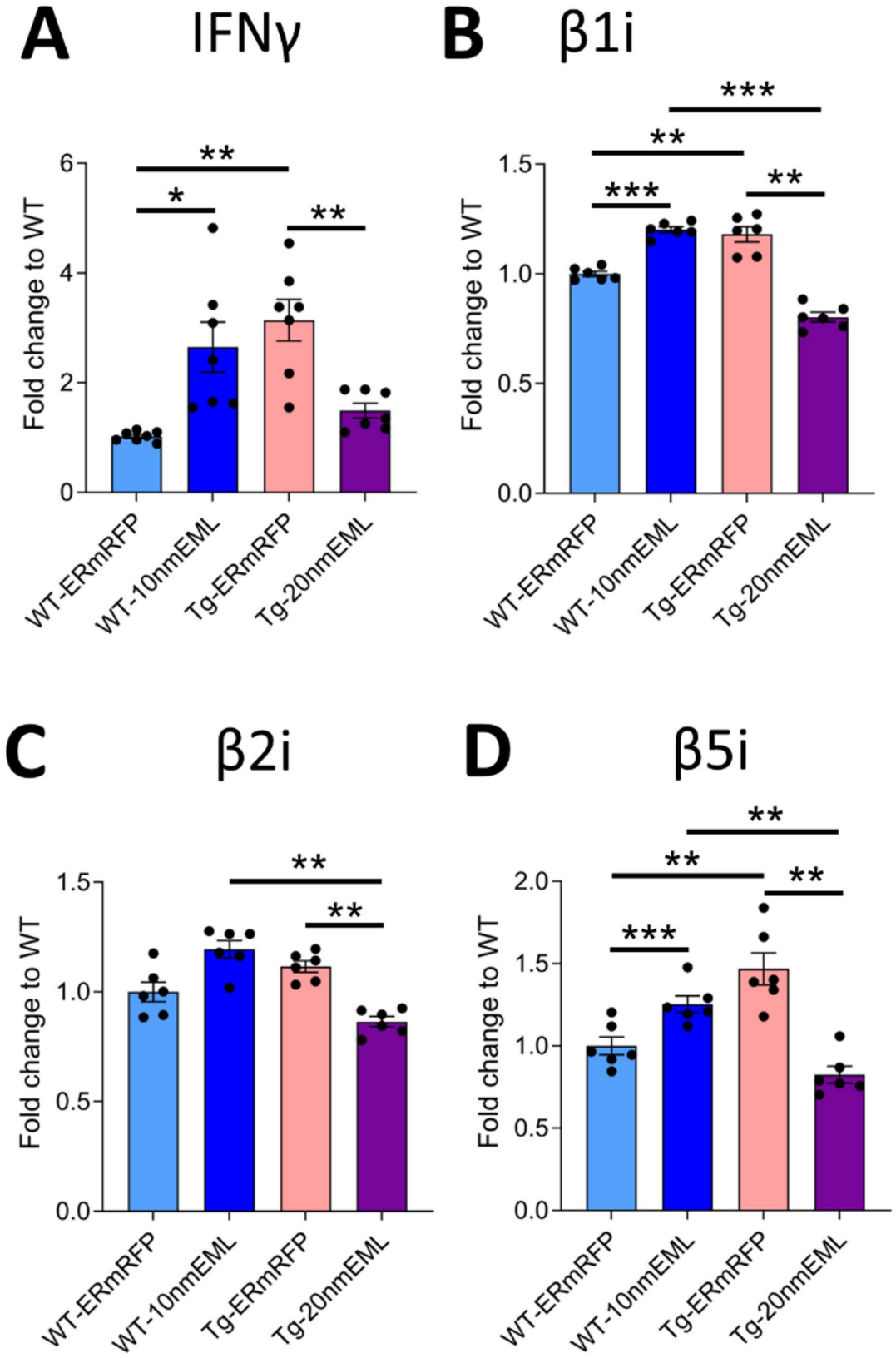

Fig. 4 Transcriptional effects of MERCS stabilization in WT- and 3Tg-iAstro on INFγ and immunoproteasome. Transcripts of *Ifng*, *Psmb9*, *Psmb10* and *Psmb8* genes coding, respectively for INFγ (**A**), β1i (**B**), β2i (**C**) and β5i (**D**) were assessed by real-time PCR using specific oligonucleotide primers in WT-iAstro cells (transfected with ER-mRFP or 10 nm-EML) and Tg-iAstro (transfected with ER-mRFP or 20 nm-EML). Data are shown as mean ± SEM for three independent experiments performed in duplicates. (* $p < 0.05$, ** $p < 0.01$, *** $p < 0.001$)

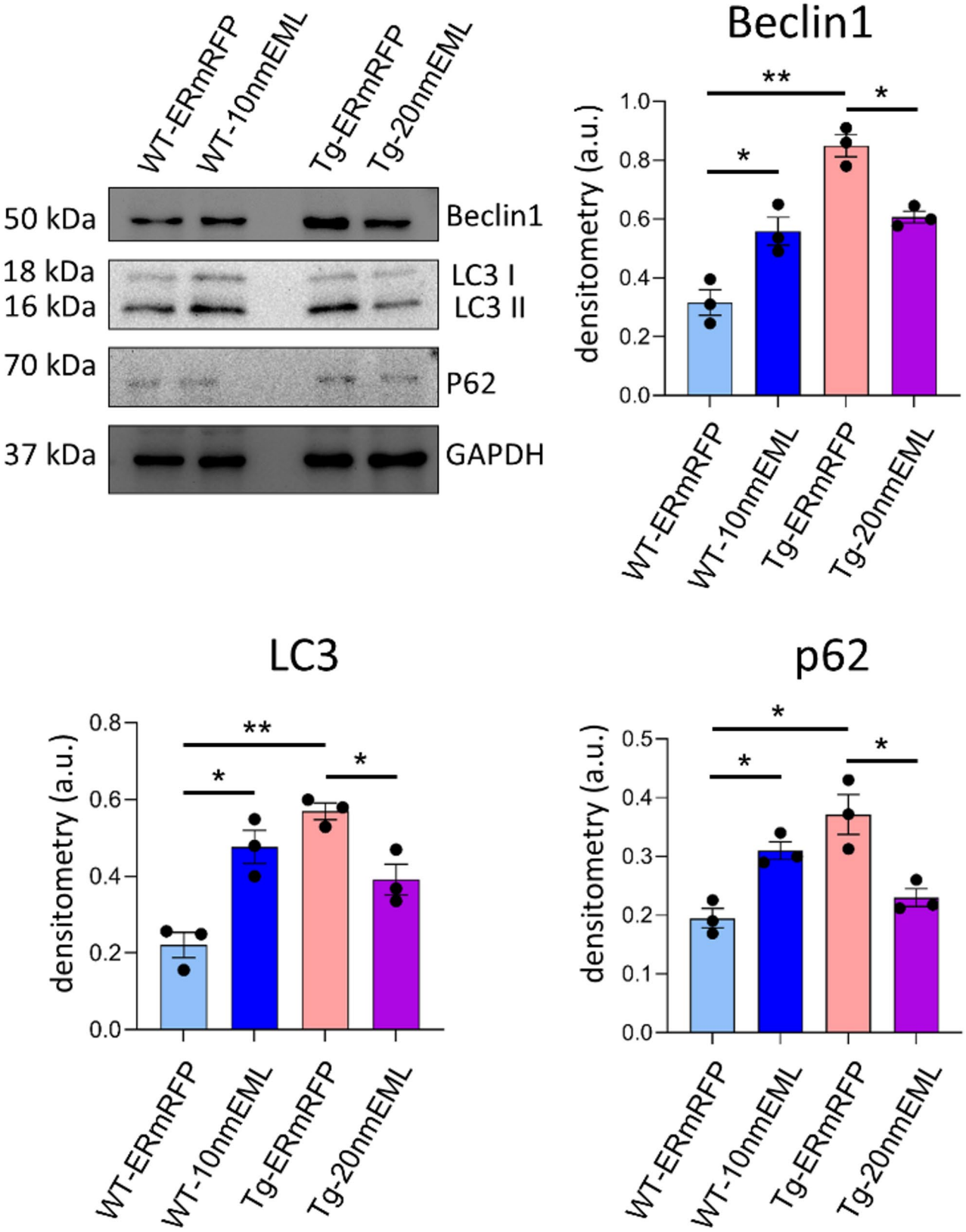

Fig. 5 Protein expression of autophagic markers. Representative western blotting images of beclin 1, LC3 II and p62 levels in WT-ERmRFP, WT-10nmEML, Tg-ERmRFP, and Tg-20nmEML hippocampal astrocytes. Mean ± SEM densitometry of each target protein normalized by GAPDH from three independent experiments is reported and expressed as arbitrary units (a.u.). (*$p < 0.05$, **$p < 0.01$, using one-way ANOVA, followed by the Bonferroni test)

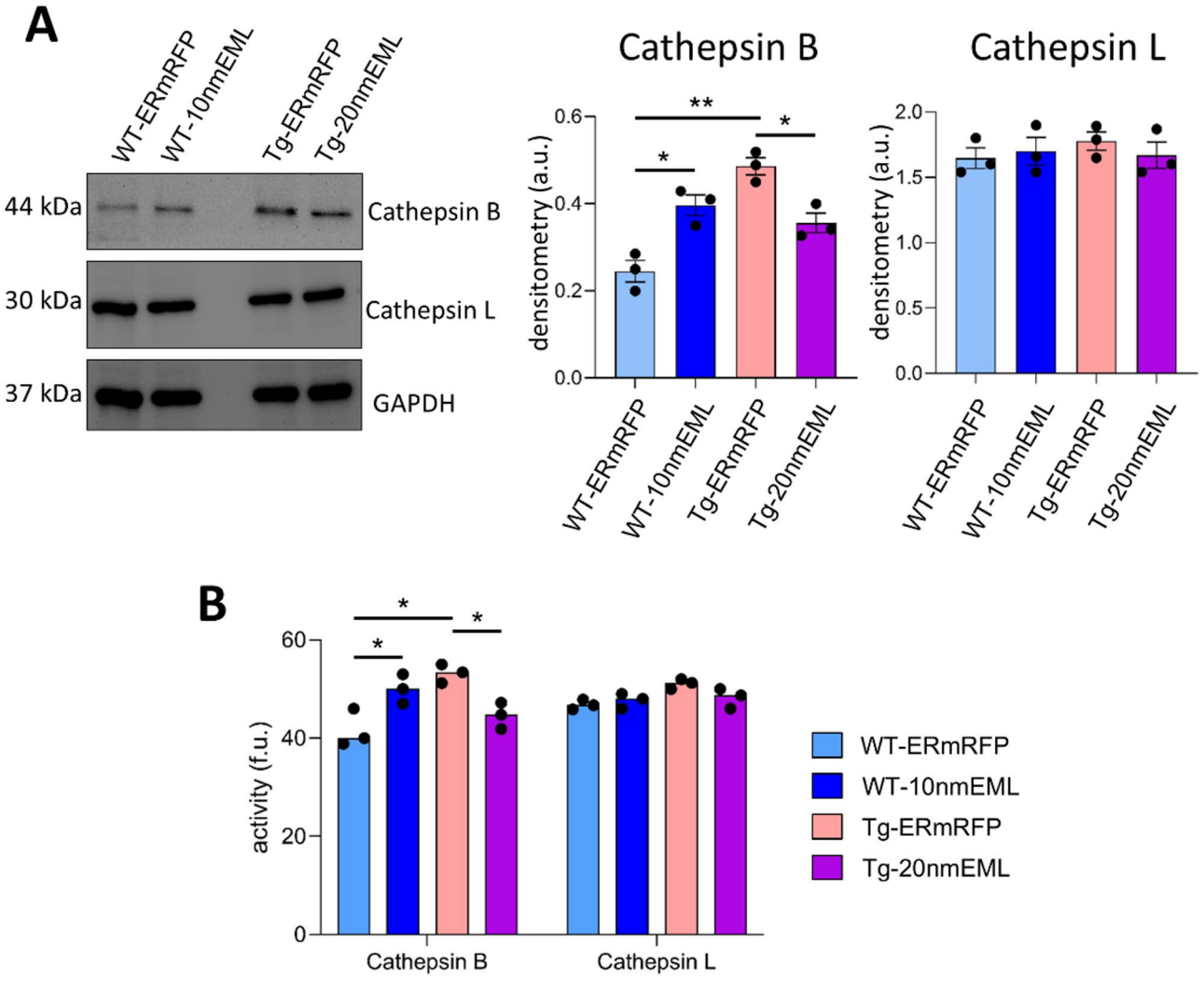

Fig. 6 Expression and activity of lysosomal enzymes. WT-iAstro were transfected with ER-mRFP or 10 nm-EML; Tg-iAstro were transfected with ER-mRFP or 20 nm-EML. (**A**) Cathepsin B and cathepsin L representative western blotting; mean ± SEM densitometry of each target protein normalized by GAPDH from three independent experiments is reported and expressed as arbitrary units (a.u.). (**B**) Cathepsin B and cathepsin L enzymatic activities are expressed as mean ± SEM fluorescence units (f.u.), (*$p < 0.05$, **$p < 0.01$, using one-way ANOVA, followed by the Bonferroni test)

the cytosol, producing equimolar amounts of GFP-LC3, which after conjugation with phosphatidylethanolamine [PE] is localized to autophagosomes and is degraded after autophagosome-lysosome fusion, and RFP, which remains in the cytoplasm as a reference. In basal conditions (no CQ treatment), GFP-LC3 shows prevalently a diffuse-cytosolic pattern in both WT-iAstro and 3Tg-iAstro cells with rare and small GFP puncta (Supplementary Fig. 2). However, after CQ treatment (20 μM, 24 h), most of WT-iAstro cells (75.26%) present numerous and bright puncta/vesicles formed by PE-conjugated and autophagosome-localized GFP-LC3, while in 24.74% of cells no puncta-vesicles were detected and GFP-LC3 presented diffuse-cytosolic localization (Fig. 7, WT-iAstro-BFP). Then, we determined percentage of cells presenting punctate-vesicular GFP-LC3 pattern in Tg-iAstro cells, and found that in most of cells (67.49%) GFP-LC3 remained in the cytosol and only 32.51% of cells presented punctate-vesicular pattern (Fig. 7, Tg-iAstro-BFP). Significant reduction of cells with punctate-vesicular GFP-LC3 in Tg-iAstro cells clearly indicate on the impairment of autophagic flux. Next, we explored the effect of 10 nm-BFP or 20 nm-BFP overexpression in WT-iAstro and Tg-iAstro, respectively. We found that WT-iAstro, transfected with 10 nm-BFP, showed a significant reduction of cells with punctate-vesicular GFP-LC3 pattern (44.85%, $p < 0.0001$ compared with WT-iAstro-ER-BFP), while Tg-iAstro, transfected with 20 nm-BFP showed partial but highly significant recovery of cells with punctate-vesicular GFP-LC3 localization (51.69%, $p < 0.0001$ compared with Tg-iAstro-ER-BFP) (Fig. 7). These results suggest that first, autophagic flux is impaired in Tg-iAstro

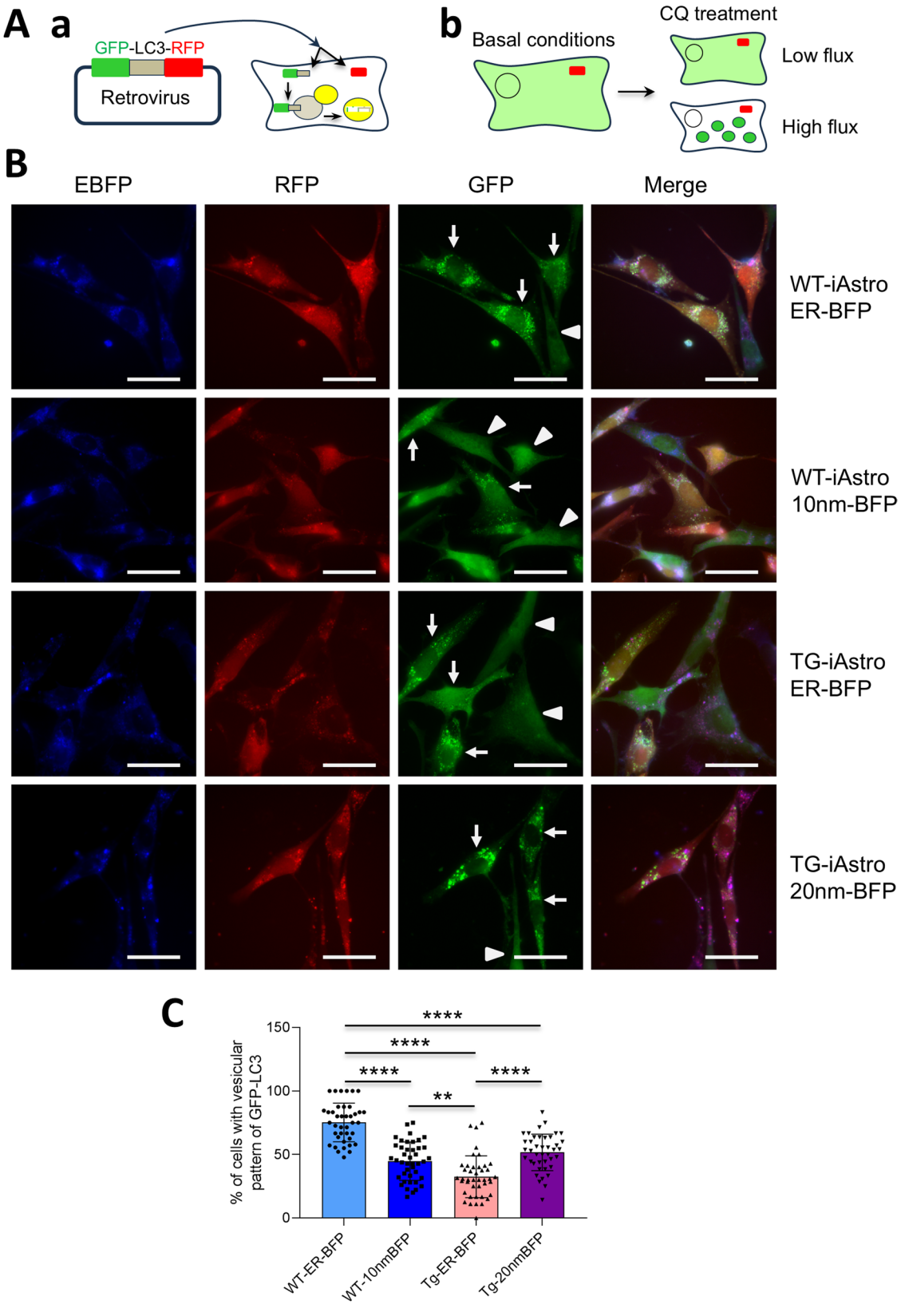

Fig. 7 (See legend on next page.)

(See figure on previous page.)

Fig. 7 Autophagic flux is impaired in Tg-iAstro and is partially rescued by 20 nm linker. (**Aa**) Scheme depicting principle of action of GFP-LC3-RFP probe. When transduced inside the cell, the probe is processed by the endogenous ATG4 family proteases that cleave the peptide bond after the C-terminal glycine of LC3 in the cytosol, producing equimolar amounts of GFP-LC3, which after conjugation with phosphatidylethanolamine is localized to autophagosomes and is degraded after autophagosome-lysosome fusion, and RFP, which remains in the cytoplasm as a reference. (**Ab**) Scheme depicting principle of measurement of autophagic flux using GFP-LC3-RFP probe. In basal conditions, at a low rate of autophagic flux, GFP-LC3 is localized to the cytosol with a diffuse pattern of distribution; upon treatment with chloroquine (20 μM, 24 h), in cells with high autophagic flux GFP-LC3 localizes into autophagosomes, while in cells with low autophagic flux, maintain cytosolic localization. The percentage of cells with the autophagosome localization of the probe is used for estimation of linkers' effect on autophagic flux. (**B**) Representative microscopy fields showing WT-iAstro and Tg-iAstro cells stably transduced with GFP-LC3-RFP probe and transiently transfected with ER-BFP (both lines) and with 10 nm-BFP and 20 nm-BFP, respectively. Arrows indicate cells with high autophagic flux rate (autophagosome localization of GFP-LC3); arrowheads indicate cells with low autophagic flux (cytosolic pattern of GFP-LC3). (**C**) Quantification of autophagic flux in WT-iAstro and Tg-iAstro expressing ER-BFP (both lines) and 10 nm-BFP and 20 nm-BFP, respectively. Data are expressed as mean ± SEM of 40–42 fields per condition (with a total of 437, 539, 790 and 510 cells for WT-iAstro -ER-BFP, WT-iAstro – 10nmBFP, Tg-iAstro-ER-BFP, and Tg-iAstro-20 nm-BFP, respectively) collected from three independent experiments. (**$p < 0.01$, ****$p < 0.0001$, using one-way ANOVA, followed by the Tukey post-hoc test). Bar = 25 μM

as compared with WT-iAstro, and secondly, autophagic flux can be efficiently modulated by modifying the distance between the ER and mitochondria.

20 nm-EML or pharmacological activation of MCU rescue mitochondrial Ca^{2+}uptake and global protein synthesis in AD astrocytes

Recently, we reported that in AD astrocytes, the proteostasis is impaired with proteasome inhibition and autophagic compensatory activation [9]. In the same hippocampal astrocytes, bioenergetic deficit was previously associated with reduced mitochondrial Ca^{2+} uptake due to the shortened distance between ER and mitochondria compared to healthy astrocytes [13, 35]. Therefore, the presented above rescue of protein degradation mechanisms in 3Tg-iAstro cells by the stabilization of the interaction between ER and mitochondria at 20 nm, potentially, may be mediated by at least two mechanisms: (i) normalization of mitochondrial Ca^{2+} uptake [31] and (ii) Ca^{2+}-independent rearrangement of MERCS proteins at the 20 nm distance between the organelles. Mitochondrial Ca^{2+} uptake depends on the activity of the highly selective channel mitochondrial calcium uniporter (MCU). Recently, FDA-approved and clinically relevant pharmacological modulators of mitochondrial Ca^{2+} uniporter (MCU) were identified [56]. Therefore, it was important (i) to discriminate Ca^{2+}-dependent and Ca^{2+}-independent effects of 20 nm-EML expression in 3Tg-iAstro, and (ii) to test if FDA-approved pharmacological modulators may be useful for normalization of AD-related dysproteostasis.

First of all, we assessed if, similarly to other tested cells [31], mitochondrial Ca^{2+} uptake may be modulated by ER-mitochondrial distance stabilization. We found that 10 nm-EML expressed in WT-iAstro dramatically reduced, while 20 nm-EML expressed in 3Tg-iAstro cells fully rescued ATP-induced Ca^{2+} signals in mitochondrial matrix as detected using 4mtD3cpv FRET-based genetically-encoded Ca^{2+} indicator [43] (Fig. 8A).

Next, we tested if pharmacological modulators of MCU, namely the inhibitor benzethonium chloride and activator amorolfine [56], could reproduce the effects of ER-mitochondrial linkers on mitochondrial Ca^{2+} uptake. Figure 8B shows that benzethonium (inhibitor) significantly reduced ATP-induced Ca^{2+} signals in WT-iAstro, while amorolfine (activator) increased and fully rescued mitochondrial Ca^{2+} uptake in 3Tg-iAstro cells (Fig. 8C). These results suggest that mitochondrial Ca^{2+} uptake and Ca^{2+}-dependent AD-related alterations may be rescued by pharmacological activation of MCU activity.

Activation of mitochondrial Ca^{2+}uniporter partially rescues proteasomal degradation and autophagy

To investigate if the rescue of protein degradation mechanisms in 3Tg-iAstro cells by the stabilization of the interaction between the ER and mitochondria at 20 nm was due to the correction of mitochondrial calcium uptake, we undertook a pharmacological approach. In particular, we investigated if the pharmacological modulation of MCU could reproduce the AD-liked impairment of proteasomal machinery in WT-iAstro and/or rescue the impairment in 3Tg-iAstro. 20 S proteasome ChT-L, T-L, and BrAAP activities and 26 S ChT-L activity were significantly reduced in WT-iAstro treated with the inhibitor of mitochondria Ca^{2+} uptake, compared to the WT-iAstro control cells (Fig. 9A and B), with a parallel accumulation of ubiquitin conjugates (Fig. 9C).

The same proteasomal activities were partially but significantly restored in 3Tg-iAstro treated with activator of mitochondria Ca^{2+} uptake with respect to untreated 3Tg-iAstro cells (Fig. 9A and B), in line with reduced levels of ubiquitin conjugates (Fig. 9C), confirming the crucial importance of a proper mitochondrial Ca^{2+} uptake in MERCS. Interestingly, INFγ levels, which are higher in Tg-iAstro compared to WT-iAstro, were not affected by the drugs (Fig. 9D), suggesting that the IFNγ-dependent conversion of the constitutive proteasome to immunoproteasome does not depend on the impairment of mitochondrial Ca^{2+} signals.

Interestingly, the mitochondrial Ca^{2+} uptake positive modulator significantly decreased the levels of p62 and beclin-1 in 3Tg-iAstro compared with untreated cells,

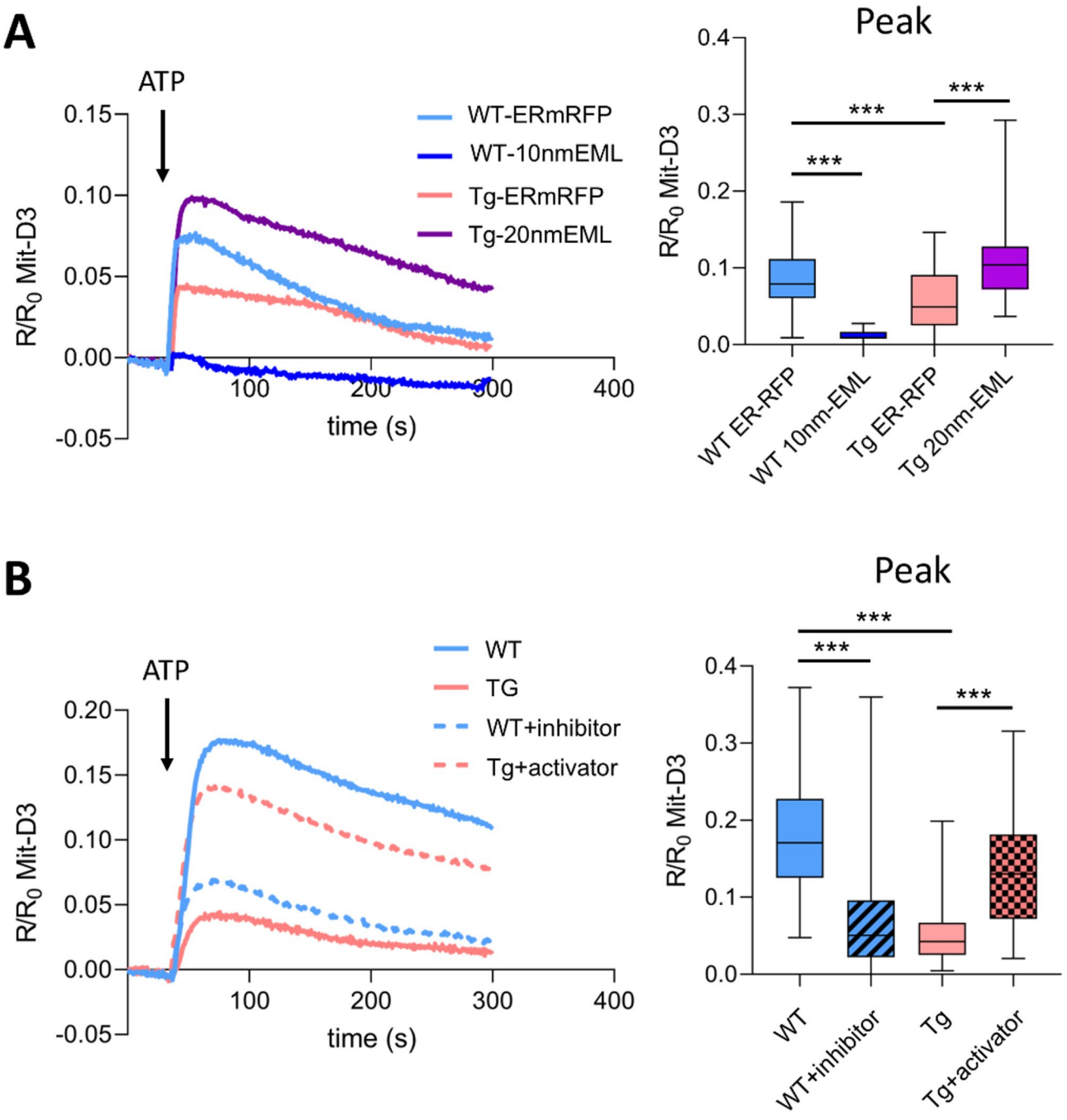

Fig. 8 Pharmacological MCU activation rescues impaired mitochondrial Ca^{2+}uptake in 3Tg-iAstro cells. (**A**), WT-iAstro expressing 10 nm-EML (WT-10nmEML) and 3Tg-iAstro expressing 20 nm-EML (Tg-20nmEML) were transfected with mitochondrial matrix-targeted 4mtD3cpv Ca^{2+} sensor. Traces show ATP (100 μM)-stimulated Ca^{2+} signals in the mitochondrial matrix. Whisker plot shows quantification of at least three independent experiments performed in triplicate (at least 50 ROI for each experimental group have been recorded). (**B**), WT-iAstro and 3Tg-iAstro cells were treated with benzethonium chloride (10 μM, activator) and amorolfine (10 μM, inhibitor), respectively. ATP-induced Ca^{2+} signals in the mitochondrial matrix were measured 24 h after treatment. Whisker plot reports data from three independent experiments performed in triplicate (at least 80 ROI for each experimental group have been recorded). (* $p < 0.05$, ** $p < 0.01$, *** $p < 0.001$)

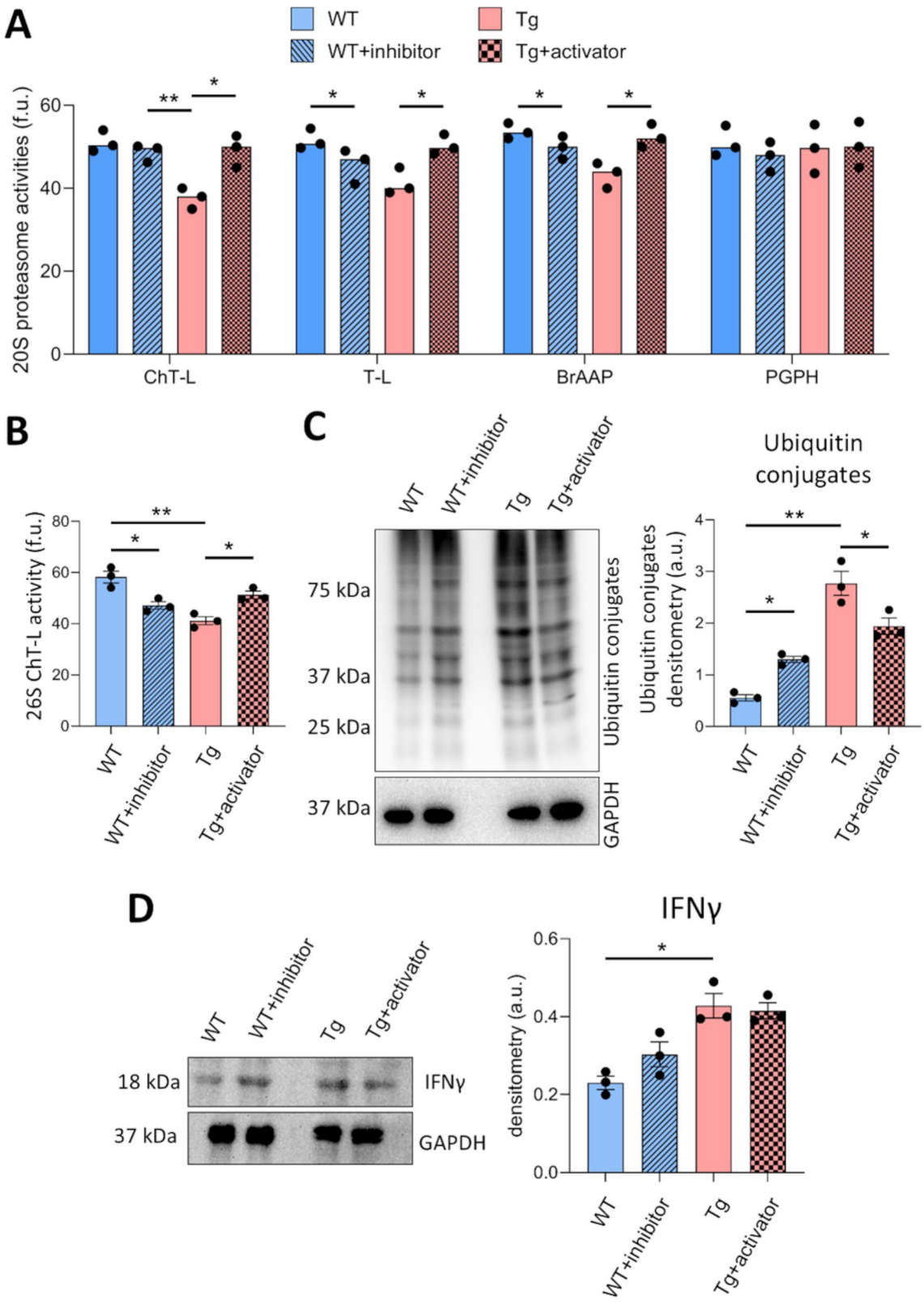

Fig. 9 (See legend on next page.)

(See figure on previous page.)

Fig. 9 Proteasomal degradation is rescued by activation of mitochondrial Ca^{2+}uniporter. (**A**) 20 S proteasome ChT-L, T-L, BrAAP and PGPH activities. (**B**) 26 S ChT-L proteasome activity in WT-iAstro (WT), WT-iAstro treated with inhibitor of mitochondria Ca^{2+} uptake (WT-iAstro + MCU inhibitor, WT + inh), 3Tg-iAstro, 3Tg-iAstro treated with activator of mitochondria Ca^{2+} uptake (Tg-iAstro + MCU activator, Tg + act). **(C)** Representative immunoblot of ubiquitin conjugates and densitometry normalized by GAPDH, expressed as arbitrary units (a.u., mean ± SEM, from three independent experiments). (**D**) IFNγ inflammatory cytokine. Densitometry of target proteins normalized by GAPDH derive from three independent experiments and are expressed as arbitrary units (a.u.). (*$p < 0.05$, **$p < 0.01$ using one-way ANOVA, followed by the Bonferroni test)

suggesting partial restoration of autophagic function, consistently with previous data [57] (Fig. 10). No difference was observed in WT-iAstro cells treated with MCU inhibitors. Taken together, our data suggest that both mitochondrial Ca^{2+}-related and Ca^{2+}-unrelated mechanisms are involved in 20 nm MERCS stabilization-dependent beneficial effects on protein dyshomeostasis.

Discussion

In this report we investigated the effects of the modulation of ER-mitochondrial interaction on the proteolytic machinery in an astrocytic model of AD, partially immortalized 3Tg-iAstro cells. The results suggest that: (i) stabilization of the interaction between ER and mitochondria at a short distance, ≈ 10 nm, in WT-iAstro reproduces the large part of the alterations in proteasomal, autophagic and lysosomal degradation machineries, as well as the reduction of ribosomal protein synthesis and mitochondrial Ca^{2+} uptake, found in 3Tg-iAstro; (ii) stabilization of the interaction at ≈ 20 nm in 3Tg-iAstro cells rescued these alterations; and (iii) application of a pharmacological modulator of mitochondrial Ca^{2+} uptake, a FDA-approved drug amorolfine, had significant positive effect, partially reverting the impairment of proteasomal activity, the accumulation of ubiquitinated proteins and the alterations in the expression of autophagic markers.

Alterations of protein homeostasis are an intrinsic feature of AD, being linked to the accumulation of misfolded and/or aggregated β-amyloid (Aβ) peptides and hyperphosphorylated tau proteins [15, 58, 59]. Early research postulated that amyloid precursor protein (APP) is located and processed at the plasma membrane, giving raise to extracellular Aβ deposits, known as senile plaques, an AD hallmark [60–62]. However, a growing number of reports suggests that Aβ is first produced and accumulated inside the cells [63, 64], and APP, together with the APP proteolytic enzymes, is located on the membranes of intracellular organelles such as the ER and/or mitochondria [65–70]. Later research suggested that the APP processing, inside the cell, occurs at the specific regions of the ER called the mitochondria-associated ER membranes (MAMs), the portions of the ER, closely adjacent to the OMM [21, 34, 71], giving the origin to the hypothesis of the involvement of the MERCS in AD pathogenesis [20, 30, 33]. A bi-directional interaction between the APP-processing machinery and MERCS has been suggested. On the one hand MERCS host AD related proteins, on the other hand mislocalized mutated APP and presenilins alter MERCS-associated functions, such as mitochondrial Ca^{2+} uptake and bioenergetics, and protein homeostasis. Furthermore, presenilins have been shown to tether the ER membrane to the OMM [22, 27], thereby altering the location and/or function of proteins involved in physiological MERCS functions. Last, but not least, ER stress/unfolded protein response (UPR) transducers such as PERK, IRE1a and ATF6, are also located in MERCS, and UPR mechanism is altered in AD [32, 72, 73]. A complex vicious cycle may be hypothesized starting from primary AD-related insults, involving enhanced ER-mitochondria tethering [74], MERCS-located aberrant APP processing [21], chronic low-grade ER-stress [15, 75] and dysregulation of protein degradation machinery [8, 76]. In astrocytes this may have detrimental consequences for their homeostatic and neuroprotective functions through alteration of the secreted factors [13, 77, 78], impaired astrocyte-neuron communication and development of neuroinflammation [79–81].

Our results support the increased MERCS hypothesis of AD, emphasizing that the distance between the ER and mitochondria plays a crucial role in the outcome of the increased interaction. By stabilizing ER-mitochondrial distance at 10 nm in WT astrocytes, in this study we were able to reproduce the dysregulation of proteasomal and autophagic protein degradation found in AD astrocytes. In line with this, in a previous report we showed that, in AD astrocytes, the increase of the ER-mitochondrial interaction at ≈ 10 nm resulted in an impairment of ribosomal protein synthesis due to increased phosphorylation of eukaryotic initiation factor 2α (eIF2α) [13]. Altogether, this suggests that the increased interaction between the ER and mitochondria, specifically at short distances around 10 nm, represents the central element of AD-related cell dysfunction and that MERCS represent a potential target for the development of therapeutic anti-AD strategies [30, 82–84].

Here we provide evidence that physical stabilization of the ER and mitochondria specifically at 20 nm distance in AD astrocytes not only improves mitochondrial Ca^{2+} signals, but also reverts key aspects of proteasomal and autophagic-lysosomal protein degradation. Beneficial effects of 20 nm distance include (i) a positive effect on mitochondrial Ca^{2+} uptake and bioenergetics [31], and (ii) a general effect on protein homeostasis which

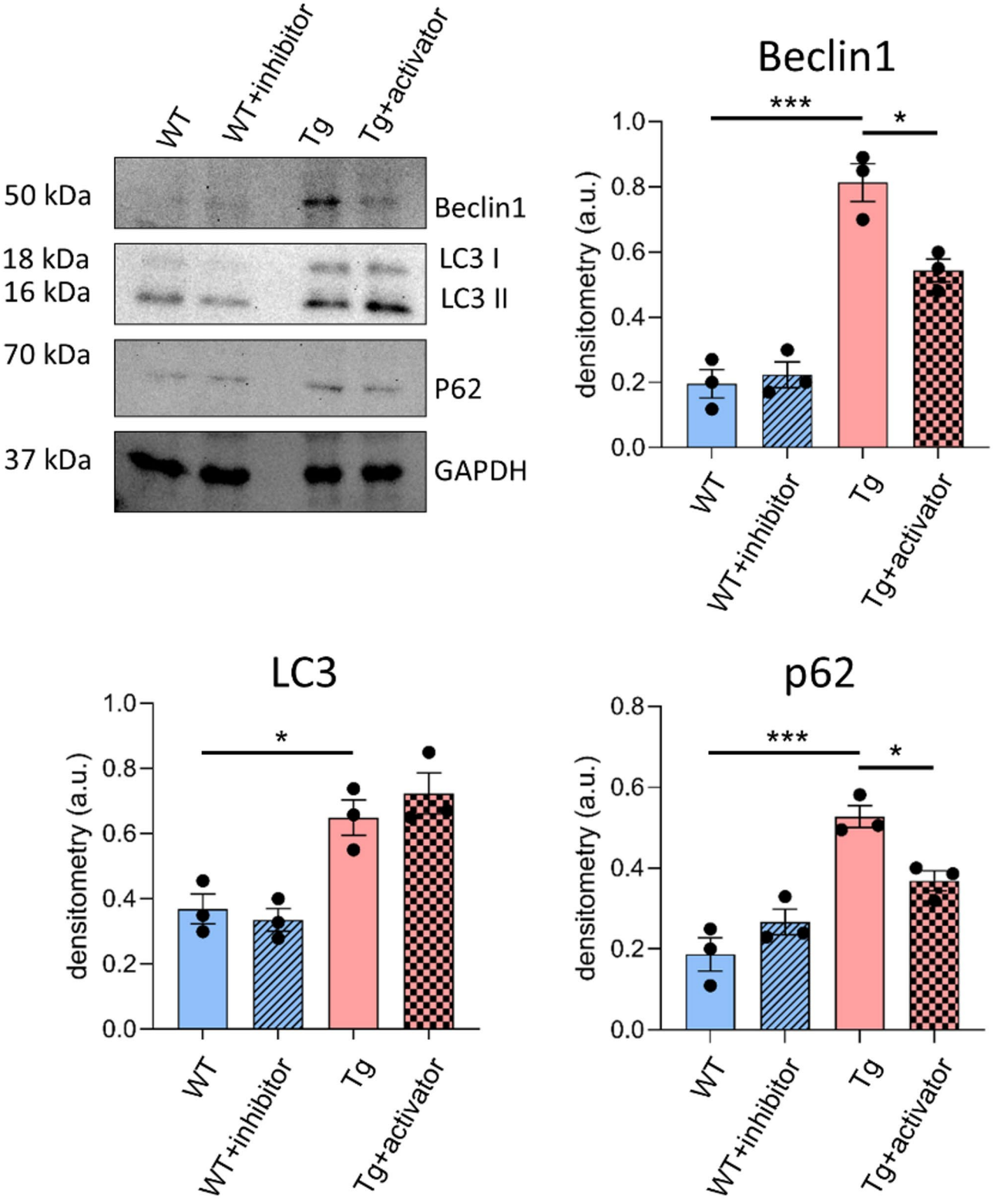

Fig. 10 Partial rescue of autophagic markers by activation of mitochondrial Ca^{2+}uniporter. Representative blots and quantifications of autophagic markers Beclin-1, LC3-II, and p62. Densitometry of target proteins normalized by GAPDH derive from three independent experiments and are expressed as arbitrary units (a.u.). (*$p < 0.05$, *** $p < 0.001$ using one-way ANOVA, followed by the Bonferroni test)

includes both local, MERCS-related, and global remodelling of protein synthesis and degradation [85]. In this complex scenario, enhancement of mitochondrial Ca^{2+} signals at 20 nm between the organelles may be mediated by both enhanced Ca^{2+} efflux from the ER due to enrichment of inositol trisphosphate receptors (IP3Rs) within 20 nm MERCS and a more efficient Ca^{2+} transfer into mitochondria due to optimization of the distance allowing efficient utilization of high [Ca^{2+}] hot-spots. Recently identified pharmacological modulators of mitochondrial Ca^{2+} uptake [56] allowed us to discriminate the effects, dependent on mitochondrial Ca^{2+} signals, from those linked to general stabilization of ER-mitochondrial interaction at 20 nm. We found that the 20 S proteasomal activity and the accumulation of ubiquitinated proteins are at least in part under the control of mitochondrial Ca^{2+} signals: these parameters were significantly ameliorated by treatment of 3Tg-iAstro cells with amorolfine. However, the levels of INFγ were insensitive to both benzethonium chloride and amorolfine, suggesting that INFγ/immunoproteasome pathway directly depends on the stabilization of ER-mitochondrial interaction.

The precise mechanism by which MERCS stabilization regulates proteasomal composition and function is currently unknown. Nevertheless, reports suggest a bidirectional interaction between MERCS and UPS. On the one hand, several authors demonstrated that mitochondrial homeostasis and membrane lipid composition may be regulated by UPS [86–88]. On the other hand, altered MERCS may affect UPS through ER stress and ER-associated protein degradation (ERAD), which eliminates misfolded/unfolded proteins via ubiquitination and proteasomal degradation. For example, increased expression of ERAD-associated proteins Sel1l (Protein Sel-1 homolog 1), Hrp1 (Ubiquitin C-terminal hydroxylase 6) and Ubqln1 (Isoform 2 of Ubiquilin-1) were found in MAMs from pre-symptomatic 3 months old APP/PS1 mouse model of AD [89].

Autophagic flux is impaired in AD [90–92]. In AD astrocytes this is translated into reduced Aβ clearance and impaired mitophagy [10, 93, 94]. Enlargement of autophagic vesicles and upregulation of LC3-II, found in 3xTg-AD astrocytes [9], suggests impaired autophagic function. We found that the stabilization of 20 nm MERCS exerts beneficial effects on the levels of autophagic markers. Moreover, using the fluorescent GFP-LC3-RFP probe, we found that the autophagic flux is significantly impaired in Tg-iAstro (expressing control plasmid) and in WT-iAstro expressing 10 nm-BFP. Strikingly, stabilization of ER-mitochondrial distance at 20 nm in Tg-iAstro significantly ameliorated the autophagic flux. Although the exact mechanism of this beneficial effect requires further investigation, reports suggest that the biogenesis of early autophagic vesicles, phagophores, initiates at MERCS [95, 96]. Although the distance for the phagophore formation, between the ER and mitochondria, was estimated to be ~50 nm [29, 95], the enlargement of the MERCS from shorter (~10 nm) to ~20 nm distance, which potentiates mitochondrial Ca^{2+} uptake [31], may be sufficient for the resolution of autophagic flux [97, 98].

The use of an astrocytic cell line, partially immortalized hippocampal astrocytes from 3xTg-AD mice [38], although represents a limitation as compared with primary astrocytes or with in vivo studies [99], allowed us to comprehensively investigate AD-related cell dysfunction using complementary and interdisciplinary methods on a uniform and standardized model [9, 13, 35, 38, 100]. The use of 3xTg-AD mice, often criticized for non-pathologically relevant overexpression of APP and tau transgenes, represents an advantage for this work due to a well characterized early AD-stage astrocytic pathology [3, 101–103]. In this frame, our previous studies, combined with the current findings, suggest that the impairment of protein synthesis and degradation in astrocytes — due to impairment of ER-mitochondrial communication — occurs early in AD pathogenesis, which may define the progression of the disease.

Conclusions

MERCS represent a promising druggable target for the development of therapy against AD, specifically for the normalization of cellular protein homeostasis. Maintenance of a correct distance between the ER and mitochondria is of paramount importance not only for mitochondrial Ca^{2+} uptake and bioenergetics [31], but also for protein synthesis and degradation pathways. Specifically, we suggest that the stabilization of the MERCS at ~20 nm may be beneficial for both cellular bioenergetics and proteostasis.

Abbreviations

AD	Alzheimer's disease
MERCS	Mitochondria–ER contact sites
OMM	Outer mitochondrial membrane
MCU	Mitochondrial calcium uniporter
EML	ER–mitochondrial linker
IFNγ	Interferon gamma
BrAAP	Branched amino acid preferring
PGPH	Peptidyl–glutamyl peptide–hydrolyzing
GAPDH	Glyceraldehyde 3–phosphate dehydrogenase
FDA	Food and drug administration
FRET	Fluorescence resonance energy transfer
eIF2α	Eukaryotic initiation factor 2α
CQ	Chloroquine
ROI	Region of interest

Supplementary Information

The online version contains supplementary material available at https://doi.org/10.1186/s13195-025-01793-9.

Supplementary Material 1

Supplementary Material 2

Acknowledgements
Not applicable.

Author contributions
Conceptualization: GD, AG, AME, LT, DL, LB; Investigation: GD, CG, LT, LB, JM, ET; Funding acquisition: GD, LT, AME, DL; Resources: AG, AME, DL; Writing - Original Draft: AME, DL, LB; Writing - Review & Editing: GD, CG, LT, AME, DL, LB, JM, ET.

Funding
EMBO short-term fellowship ASTF9854 (GD); CRT Foundation grant 1393–2017 (LT); FAR-2019 from the Università del Piemonte Orientale (DL); This publication is part of the project PNRR-MCNT2-2023-12377363, which has received funding from NextGeneration EU - Ministry of Health – M6C2 2.1, CUP C13C24000440007; PRC collaborative funds from Jilin Agricultural University (AME).

Data availability
No datasets were generated or analysed during the current study.

Declarations

Ethics approval and consent to participate
Not applicable.

Consent for publication
Not applicable.

Competing interests
The authors declare no competing interests.

Author details
[1]Department of Pharmaceutical Sciences, Università del Piemonte Orientale, Via Bovio 6, Novara 28100, Italy
[2]School of Biosciences and Veterinary Medicine, University of Camerino, Via Gentile III da Varano, Camerino, MC 62032, Italy
[3]Experimental Neurology Unit, School of Medicine and Surgery, University of Milano- Bicocca, Milan, Italy
[4]Department of Drug Science and Technology, University of Turin, Turin, Italy
[5]Present address: U1215 NeuroCentre Magendie, INSERM, Bordeaux 33077, France

Received: 24 January 2025 / Accepted: 20 June 2025
Published online: 04 July 2025

References

1. Ihara Y, Morishima-Kawashima M, Nixon R. The ubiquitin-proteasome system and the autophagic-lysosomal system in Alzheimer disease. Cold Spring Harb Perspect Med. 2012;2:a006361.
2. Orre M, Kamphuis W, Dooves S, Kooijman L, Chan ET, Kirk CJ, et al. Reactive glia show increased immunoproteasome activity in Alzheimer's disease. Brain J Neurol. 2013;136:1415–31.
3. Lim D, Rodríguez-Arellano JJ, Parpura V, Zorec R, Zeidán-Chuliá F, Genazzani AA, et al. Calcium signalling toolkits in astrocytes and spatio-temporal progression of Alzheimer's disease. Curr Alzheimer Res. 2016;13:359–69.
4. Grolla AA, Fakhfouri G, Balzaretti G, Marcello E, Gardoni F, Canonico PL, et al. Aβ leads to Ca^{2+} signaling alterations and transcriptional changes in glial cells. Neurobiol Aging. 2013;34:511–22.
5. Hartlage-Rübsamen M, Zeitschel U, Apelt J, Gärtner U, Franke H, Stahl T, et al. Astrocytic expression of the Alzheimer's disease beta-secretase (BACE1) is stimulus-dependent. Glia. 2003;41:169–79.
6. Jin SM, Cho HJ, Kim YW, Hwang JY, Mook-Jung I. Aβ-induced Ca(2+) influx regulates astrocytic BACE1 expression via calcineurin/NFAT4 signals. Biochem Biophys Res Commun. 2012;425:649–55.
7. Cecarini V, Bonfili L, Cuccioloni M, Mozzicafreddo M, Rossi G, Buizza L, et al. Crosstalk between the ubiquitin-proteasome system and autophagy in a human cellular model of Alzheimer's disease. Biochim Biophys Acta. 2012;1822:1741–51.
8. Cecarini V, Bonfili L, Cuccioloni M, Mozzicafreddo M, Angeletti M, Keller JN, et al. The fine-tuning of proteolytic pathways in Alzheimer's disease. Cell Mol Life Sci CMLS. 2016;73:3433–51.
9. Gong C, Bonfili L, Zheng Y, Cecarini V, Cuccioloni M, Angeletti M, et al. Immortalized Alzheimer's disease astrocytes: characterization of their proteolytic systems. Mol Neurobiol. 2023;60:2787–800.
10. Kim S, Chun H, Kim Y, Kim Y, Park U, Chu J, et al. Astrocytic autophagy plasticity modulates Aβ clearance and cognitive function in Alzheimer's disease. Mol Neurodegener. 2024;19:55.
11. Ries M, Sastre M. Mechanisms of Aβ clearance and degradation by glial cells. Front Aging Neurosci. 2016;8:160.
12. Jha MK, Kim J-H, Song GJ, Lee W-H, Lee I-K, Lee H-W, et al. Functional dissection of astrocyte-secreted proteins: implications in brain health and diseases. Prog Neurobiol. 2018;162:37–69.
13. Tapella L, Dematteis G, Moro M, Pistolato B, Tonelli E, Vanella VV, et al. Protein synthesis Inhibition and loss of homeostatic functions in astrocytes from an Alzheimer's disease mouse model: a role for ER-mitochondria interaction. Cell Death Dis. 2022;13:878.
14. Verkhratsky A, Matteoli M, Parpura V, Mothet J-P, Zorec R. Astrocytes as secretory cells of the central nervous system: idiosyncrasies of vesicular secretion. EMBO J. 2016;35:239–57.
15. Lim D, Tapella L, Dematteis G, Genazzani AA, Corazzari M, Verkhratsky A. The Endoplasmic reticulum stress and unfolded protein response in Alzheimer's disease: a calcium dyshomeostasis perspective. Ageing Res Rev. 2023;87:101914.
16. Verkhratsky A, Parpura V, Li B, Scuderi C. Astrocytes: the housekeepers and guardians of the CNS. Adv Neurobiol. 2021;26:21–53.
17. Verkhratsky A, Nedergaard M. The homeostatic astroglia emerges from evolutionary specialization of neural cells. Philos Trans R Soc Lond B Biol Sci. 2016;371.
18. Barazzuol L, Giamogante F, Calì T. Mitochondria associated membranes (MAMs): architecture and physiopathological role. Cell Calcium. 2021;94:102343.
19. Hayashi T, Rizzuto R, Hajnoczky G, Su T-P. MAM: more than just a housekeeper. Trends Cell Biol. 2009;19:81–8.
20. Area-Gomez E, Del Carmen Lara Castillo M, Tambini MD, Guardia-Laguarta C, de Groof AJC, Madra M, et al. Upregulated function of mitochondria-associated ER membranes in Alzheimer disease. EMBO J. 2012;31:4106–23.
21. Area-Gomez E, de Groof A, Bonilla E, Montesinos J, Tanji K, Boldogh I, et al. A key role for MAM in mediating mitochondrial dysfunction in Alzheimer disease. Cell Death Dis. 2018;9:335.
22. Filadi R, Greotti E, Turacchio G, Luini A, Pozzan T, Pizzo P. Presenilin 2 modulates endoplasmic reticulum-mitochondria coupling by tuning the antagonistic effect of mitofusin 2. Cell Rep. 2016;15:2226–38.
23. Hedskog L, Pinho CM, Filadi R, Rönnbäck A, Hertwig L, Wiehager B, et al. Modulation of the endoplasmic reticulum-mitochondria interface in Alzheimer's disease and related models. Proc Natl Acad Sci U S A. 2013;110:7916–21.
24. Leal NS, Dentoni G, Schreiner B, Naia L, Piras A, Graff C, et al. Amyloid B-Peptide increases mitochondria-endoplasmic reticulum contact altering mitochondrial function and autophagosome formation in Alzheimer's disease-related models. Cells. 2020;9:2552.
25. Perreault S, Bousquet O, Lauzon M, Paiement J, Leclerc N. Increased association between rough endoplasmic reticulum membranes and mitochondria in transgenic mice that express P301L tau. J Neuropathol Exp Neurol. 2009;68:503–14.
26. Tambini MD, Pera M, Kanter E, Yang H, Guardia-Laguarta C, Holtzman D, et al. ApoE4 upregulates the activity of mitochondria-associated ER membranes. EMBO Rep. 2016;17:27–36.
27. Zampese E, Fasolato C, Kipanyula MJ, Bortolozzi M, Pozzan T, Pizzo P. Presenilin 2 modulates endoplasmic reticulum (ER)-mitochondria interactions and Ca2 + cross-talk. Proc Natl Acad Sci U S A. 2011;108:2777–82.
28. Csordás G, Renken C, Várnai P, Walter L, Weaver D, Buttle KF, et al. Structural and functional features and significance of the physical linkage between ER and mitochondria. J Cell Biol. 2006;174:915–21.
29. Giacomello M, Pellegrini L. The coming of age of the mitochondria-ER contact: a matter of thickness. Cell Death Differ. 2016;23:1417–27.

30. Lim D, Dematteis G, Tapella L, Genazzani AA, Calì T, Brini M, et al. Ca2 + handling at the mitochondria-ER contact sites in neurodegeneration. Cell Calcium. 2021;98:102453.
31. Dematteis G, Tapella L, Casali C, Talmon M, Tonelli E, Reano S, et al. ER-mitochondria distance is a critical parameter for efficient mitochondrial Ca2 + uptake and oxidative metabolism. Commun Biol. 2024;7:1294.
32. Carreras-Sureda A, Kroemer G, Cardenas JC, Hetz C. Balancing energy and protein homeostasis at ER-mitochondria contact sites. Sci Signal. 2022;15:eabm7524.
33. Paillusson S, Stoica R, Gomez-Suaga P, Lau DHW, Mueller S, Miller T, et al. There's something wrong with my MAM; the ER-mitochondria axis and neurodegenerative diseases. Trends Neurosci. 2016;39:146–57.
34. Schon EA, Area-Gomez E. Mitochondria-associated ER membranes in Alzheimer disease. Mol Cell Neurosci. 2013;55:26–36.
35. Dematteis G, Vydmantaitė G, Ruffinatti FA, Chahin M, Farruggio S, Barberis E, et al. Proteomic analysis links alterations of bioenergetics, mitochondria-ER interactions and proteostasis in hippocampal astrocytes from 3xTg-AD mice. Cell Death Dis. 2020;11:645.
36. Calì T, Brini M. Quantification of organelle contact sites by split-GFP-based contact site sensors (SPLICS) in living cells. Nat Protoc. 2021;16:5287–308.
37. Cieri D, Vicario M, Giacomello M, Vallese F, Filadi R, Wagner T, et al. SPLICS: a split green fluorescent protein-based contact site sensor for narrow and wide heterotypic organelle juxtaposition. Cell Death Differ. 2018;25:1131–45.
38. Rocchio F, Tapella L, Manfredi M, Chisari M, Ronco F, Ruffinatti FA, et al. Gene expression, proteome and calcium signaling alterations in immortalized hippocampal astrocytes from an Alzheimer's disease mouse model. Cell Death Dis. 2019;10:24.
39. Csordás G, Várnai P, Golenár T, Roy S, Purkins G, Schneider TG, et al. Imaging interorganelle contacts and local calcium dynamics at the ER-mitochondrial interface. Mol Cell. 2010;39:121–32.
40. Kaizuka T, Morishita H, Hama Y, Tsukamoto S, Matsui T, Toyota Y, et al. An autophagic flux probe that releases an internal control. Mol Cell. 2016;64:835–49.
41. Bonfili L, Cecarini V, Cuccioloni M, Angeletti M, Flati V, Corsetti G, et al. Essential amino acid mixtures drive cancer cells to apoptosis through proteasome inhibition and autophagy activation. FEBS J. 2017;284:1726–37.
42. Tchoupe JR, Moreau T, Gauthier F, Bieth JG. Photometric or fluorometric assay of cathepsin B, L and H and papain using substrates with an aminotrifluoromethylcoumarin leaving group. Biochim Biophys Acta. 1991;1076:149–51.
43. Palmer AE, Giacomello M, Kortemme T, Hires SA, Lev-Ram V, Baker D, et al. Ca2 + indicators based on computationally redesigned calmodulin-peptide pairs. Chem Biol. 2006;13:521–30.
44. Rock KL, Goldberg AL. Degradation of cell proteins and the generation of MHC class I-presented peptides. Annu Rev Immunol. 1999;17:739–79.
45. Davidson K, Pickering AM. The proteasome: a key modulator of nervous system function, brain aging, and neurodegenerative disease. Front Cell Dev Biol. 2023;11:1124907.
46. Miyauchi S, Kim SS, Jones RN, Zhang L, Guram K, Sharma S, et al. Human papillomavirus E5 suppresses immunity via inhibition of the immunoproteasome and STING pathway. Cell Rep. 2023;42:112508.
47. Heink S, Ludwig D, Kloetzel P-M, Krüger E. IFN-gamma-induced immune adaptation of the proteasome system is an accelerated and transient response. Proc Natl Acad Sci U S A. 2005;102:9241–6.
48. Raynes R, Pomatto LCD, Davies KJA. Degradation of oxidized proteins by the proteasome: distinguishing between the 20S, 26S, and immunoproteasome proteolytic pathways. Mol Aspects Med. 2016;50:41–55.
49. Rock KL, Gramm C, Rothstein L, Clark K, Stein R, Dick L, et al. Inhibitors of the proteasome block the degradation of most cell proteins and the generation of peptides presented on MHC class I molecules. Cell. 1994;78:761–71.
50. Jiang R-Q, Li Q-Q, Sheng R. Mitochondria associated ER membranes and cerebral ischemia: molecular mechanisms and therapeutic strategies. Pharmacol Res. 2023;191:106761.
51. Gomez-Suaga P, Paillusson S, Stoica R, Noble W, Hanger DP, Miller CCJ. The ER-Mitochondria tethering complex VAPB-PTPIP51 regulates autophagy. Curr Biol CB. 2017;27:371–85.
52. Kim MJ, Kim S, Reinheckel T, Krainc D. Inhibition of cysteine protease cathepsin L increases the level and activity of lysosomal glucocerebrosidase. JCI Insight. 2024;9:e169594.
53. Yuyama K, Sun H, Fujii R, Hemmi I, Ueda K, Igeta Y. Extracellular vesicle proteome unveils cathepsin B connection to Alzheimer's disease pathogenesis. Brain J Neurol. 2024;147:627–36.
54. Drobny A, Prieto Huarcaya S, Dobert J, Kluge A, Bunk J, Schlothauer T, et al. The role of lysosomal cathepsins in neurodegeneration: mechanistic insights, diagnostic potential and therapeutic approaches. Biochim Biophys Acta Mol Cell Res. 2022;1869:119243.
55. Janikiewicz J, Szymański J, Malinska D, Patalas-Krawczyk P, Michalska B, Duszyński J, et al. Mitochondria-associated membranes in aging and senescence: structure, function, and dynamics. Cell Death Dis. 2018;9:332.
56. De Mario A, Tosatto A, Hill JM, Kriston-Vizi J, Ketteler R, Vecellio Reane D, et al. Identification and functional validation of FDA-approved positive and negative modulators of the mitochondrial calcium uniporter. Cell Rep. 2021;35:109275.
57. Medina DL, Ballabio A. Lysosomal calcium regulates autophagy. Autophagy. 2015;11:970–1.
58. Cheng J, North BJ, Zhang T, Dai X, Tao K, Guo J, et al. The emerging roles of protein homeostasis-governing pathways in Alzheimer's disease. Aging Cell. 2018;17:e12801.
59. Morawe T, Hiebel C, Kern A, Behl C. Protein homeostasis, aging and Alzheimer's disease. Mol Neurobiol. 2012;46:41–54.
60. Hardy J. Amyloid, the presenilins and Alzheimer's disease. Trends Neurosci. 1997;20:154–9.
61. Hardy JA, Higgins GA. Alzheimer's disease: the amyloid cascade hypothesis. Science. 1992;256:184–5.
62. Selkoe DJ. The cell biology of beta-amyloid precursor protein and presenilin in Alzheimer's disease. Trends Cell Biol. 1998;8:447–53.
63. LaFerla FM, Green KN, Oddo S. Intracellular amyloid-beta in Alzheimer's disease. Nat Rev Neurosci. 2007;8:499–509.
64. Oddo S, Caccamo A, Smith IF, Green KN, LaFerla FM. A dynamic relationship between intracellular and extracellular pools of Abeta. Am J Pathol. 2006;168:184–94.
65. Behbahani H, Pavlov PF, Wiehager B, Nishimura T, Winblad B, Ankarcrona M. Association of Omi/HtrA2 with γ-secretase in mitochondria. Neurochem Int. 2010;57:668–75.
66. Hansson CA, Frykman S, Farmery MR, Tjernberg LO, Nilsberth C, Pursglove SE, et al. Nicastrin, presenilin, APH-1, and PEN-2 form active gamma-secretase complexes in mitochondria. J Biol Chem. 2004;279:51654–60.
67. Nowakowska-Gołacka J, Czapiewska J, Sominka H, Sowa-Rogozińska N, Słomińska-Wojewódzka M. EDEM1 regulates amyloid precursor protein (APP) metabolism and amyloid-β production. Int J Mol Sci. 2021;23:117.
68. Pavlov PF, Wiehager B, Sakai J, Frykman S, Behbahani H, Winblad B, et al. Mitochondrial γ-secretase participates in the metabolism of mitochondria-associated amyloid precursor protein. FASEB J Off Publ Fed Am Soc Exp Biol. 2011;25:78–88.
69. Plácido AI, Pereira CMF, Duarte AI, Candeias E, Correia SC, Santos RX, et al. The role of endoplasmic reticulum in amyloid precursor protein processing and trafficking: implications for Alzheimer's disease. Biochim Biophys Acta. 2014;1842:1444–53.
70. Wilkins HM. Interactions between amyloid, amyloid precursor protein, and mitochondria. Biochem Soc Trans. 2023;51:173–82.
71. Del Prete D, Suski JM, Oulès B, Debayle D, Gay AS, Lacas-Gervais S, et al. Localization and processing of the amyloid-β protein precursor in mitochondria-associated membranes. J Alzheimers Dis JAD. 2017;55:1549–70.
72. Casas-Martinez JC, Samali A, McDonagh B. Redox regulation of UPR signalling and mitochondrial ER contact sites. Cell Mol Life Sci CMLS. 2024;81:250.
73. van Vliet AR, Agostinis P. Mitochondria-associated membranes and ER stress. Curr Top Microbiol Immunol. 2018;414:73–102.
74. Filadi R, Theurey P, Pizzo P. The Endoplasmic reticulum-mitochondria coupling in health and disease: molecules, functions and significance. Cell Calcium. 2017;62:1–15.
75. Lim D, Verkhratsky A. Alterations of protein homeostasis in Alzheimer's disease: beyond procrustean bed of endoplasmic reticulum stress and unfolded protein response. Neural Regen Res. 2024;19:1645–6.
76. Gadhave K, Bolshette N, Ahire A, Pardeshi R, Thakur K, Trandafir C, et al. The ubiquitin proteasomal system: a potential target for the management of Alzheimer's disease. J Cell Mol Med. 2016;20:1392–407.
77. Cassé F, Richetin K, Toni N. Astrocytes' contribution to adult neurogenesis in physiology and Alzheimer's disease. Front Cell Neurosci. 2018;12:432.
78. Preman P, Alfonso-Triguero M, Alberdi E, Verkhratsky A, Arranz AM. Astrocytes in Alzheimer's disease: pathological significance and molecular pathways. Cells. 2021;10:540.
79. Lim D, Tapella L, Dematteis G, Talmon M, Genazzani AA. Calcineurin signalling in astrocytes: from pathology to physiology and control of neuronal functions. Neurochem Res. 2023;48:1077–90.

80. Nanclares C, Baraibar AM, Araque A, Kofuji P. Dysregulation of astrocyte-neuronal communication in Alzheimer's disease. Int J Mol Sci. 2021;22:7887.
81. Uddin MS, Yu WS, Lim LW. Exploring ER stress response in cellular aging and neuroinflammation in Alzheimer's disease. Ageing Res Rev. 2021;70:101417.
82. Callens M, Loncke J, Bultynck G. Dysregulated Ca2 + homeostasis as a central theme in neurodegeneration: lessons from Alzheimer's disease and wolfram syndrome. Cells. 2022;11:1963.
83. Dentoni G, Castro-Aldrete L, Naia L, Ankarcrona M. The potential of small molecules to modulate the mitochondria-endoplasmic reticulum interplay in Alzheimer's disease. Front Cell Dev Biol. 2022;10:920228.
84. Leal NS, Martins LM. Mind the gap: mitochondria and the endoplasmic reticulum in neurodegenerative diseases. Biomedicines. 2021;9:227.
85. Tonelli E, Malecka J, Barberis E, Romano C, Pessolano E, Talmon M, et al. Remodelling of cellular protein homeostasis by enhanced ER-mitochondrial tethering. Contact Thousand Oaks Ventura Cty Calif. 2025;8:25152564251329704.
86. Alsayyah C, Ozturk O, Cavellini L, Belgareh-Touzé N, Cohen MM. The regulation of mitochondrial homeostasis by the ubiquitin proteasome system. Biochim Biophys Acta Bioenerg. 2020;1861:148302.
87. Ganji R, Paulo JA, Xi Y, Kline I, Zhu J, Clemen CS, et al. The p97-UBXD8 complex regulates ER-mitochondria contact sites by altering membrane lipid saturation and composition. Nat Commun. 2023;14:638.
88. Karbowski M, Youle RJ. Regulating mitochondrial outer membrane proteins by ubiquitination and proteasomal degradation. Curr Opin Cell Biol. 2011;23:476–82.
89. Völgyi K, Badics K, Sialana FJ, Gulyássy P, Udvari EB, Kis V, et al. Early presymptomatic changes in the proteome of mitochondria-associated membrane in the APP/PS1 mouse model of Alzheimer's disease. Mol Neurobiol. 2018;55:7839–57.
90. Barmaki H, Nourazarian A, Khaki-Khatibi F. Proteostasis and neurodegeneration: a closer look at autophagy in Alzheimer's disease. Front Aging Neurosci. 2023;15:1281338.
91. Uddin MS, Stachowiak A, Mamun AA, Tzvetkov NT, Takeda S, Atanasov AG, et al. Autophagy and Alzheimer's disease: from molecular mechanisms to therapeutic implications. Front Aging Neurosci. 2018;10:04.
92. Zhang Z, Yang X, Song Y-Q, Tu J. Autophagy in Alzheimer's disease pathogenesis: therapeutic potential and future perspectives. Ageing Res Rev. 2021;72:101464.
93. Litwiniuk A, Juszczak GR, Stankiewicz AM, Urbańska K. The role of glial autophagy in Alzheimer's disease. Mol Psychiatry. 2023;28:4528–39.
94. Mary A, Eysert F, Checler F, Chami M. Mitophagy in Alzheimer's disease: molecular defects and therapeutic approaches. Mol Psychiatry. 2023;28:202–16.
95. Hamasaki M, Furuta N, Matsuda A, Nezu A, Yamamoto A, Fujita N, et al. Autophagosomes form at ER-mitochondria contact sites. Nature. 2013;495:389–93.
96. Zhen Y, Stenmark H. Autophagosome biogenesis. Cells. 2023;12:668.
97. Chandra S, Katiyar P, Durairaj AS, Wang X. Mitochondrial calcium transport during autophagy initiation. Mitochondrial Commun. 2024;2:14–20.
98. Gherardi G, Di Marco G, Rizzuto R, Mammucari C. Crosstalk between mitochondrial Ca2 + Uptake and autophagy in skeletal muscle. Oxid Med Cell Longev. 2019;2019:1845321.
99. Galland F, Seady M, Taday J, Smaili SS, Gonçalves CA, Leite MC. Astrocyte culture models: molecular and function characterization of primary culture, immortalized astrocytes and C6 glioma cells. Neurochem Int. 2019;131:104538.
100. Tapella L, Dematteis G, Genazzani AA, De Paola M, Lim D. Immortalized hippocampal astrocytes from 3xTg-AD mice, a new model to study disease-related astrocytic dysfunction: a comparative review. Neural Regen Res. 2023;18:1672–8.
101. Olabarria M, Noristani HN, Verkhratsky A, Rodríguez JJ. Concomitant astroglial atrophy and astrogliosis in a triple transgenic animal model of Alzheimer's disease. Glia. 2010;58:831–8.
102. Yeh C-Y, Vadhwana B, Verkhratsky A, Rodríguez JJ. Early astrocytic atrophy in the entorhinal cortex of a triple transgenic animal model of Alzheimer's disease. ASN Neuro. 2011;3:271–9.
103. Lim D, Matute C, Cavaliere F, Verkhratsky A. Neuroglia in neurodegeneration: Alzheimer, Parkinson, and Huntington disease. Handb Clin Neurol. 2025;210:9–44.

Publisher's note